ANNUAL REVIEWS

Evolution and Mass Loss of Cool Aging Stars: A Daedalean Story

Leen Decin[1,2]

[1]Institute of Astronomy, KU Leuven, B-3001 Leuven, Belgium; email: Leen.Decin@kuleuven.be
[2]University of Leeds, School of Chemistry, Leeds LS2 9JT, United Kingdom

Keywords

Abstract

A multitude of phenomena—such as the chemical enrichment of the Universe, the mass spectrum of planetary nebulae, white dwarfs and gravitational wave progenitors, the frequency distribution of supernovae, the fate of exoplanets, etc.—are highly regulated by the amounts of mass that stars expel through a powerful wind. For more than half a century, these winds of cool aging stars have been interpreted within the common interpretive framework of 1D models. I here discuss how that framework now appears to be highly problematic.

- Current 1D mass-loss rate formulae differ by orders of magnitude, rendering contemporary stellar evolution predictions highly uncertain.

These stellar winds harbor 3D complexities that bridge 23 orders of magnitude in scale, ranging from the nanometer up to thousands of astronomical units. We need to embrace and understand these 3D spatial realities if we aim to quantify mass loss and assess its effect on stellar evolution. We therefore need to gauge the following:

- The 3D life of molecules and solid-state aggregates: The gas-phase clusters that form the first dust seeds are not yet identified. This limits our ability to predict mass-loss rates using a self-consistent approach.
- The emergence of 3D clumps: They contribute in a nonnegligible way to the mass loss, although they seem of limited importance for the wind-driving mechanism.
- The 3D lasting impact of a (hidden) companion: Unrecognized binary interaction has biased previous mass-loss rate estimates toward values that are too large.

Only then will it be possible to drastically improve our predictive power of the evolutionary path in 4D (classical) spacetime of any star.

Contents

1. DETERMINISTIC AND CONCEPTUAL PERSPECTIVE

Stars are born and die. Much of humankind's attention and imagination is directed toward the star-forming process, the phase during which new planets are formed around young stars that harbor the tantalizing potential for new life forms to arise. Traditionally, the end-phases of stellar evolution have received much less attention. Supernovae (SNe), neutron stars, and black holes avoid the perception of being unglamorous old stars but the research field focusing on the late stages of stellar evolution of low- and intermediate-mass stars is far less blessed by public excitement.

Cool aging stars possess, however, some characteristics that turn them into key objects for both deterministic and conceptual questions in the broad field of astrophysics. The deterministic facet is linked to the chemical enrichment of our Universe. These stars are nuclear power plants that create new atoms inside their hot dense cores, including carbon, the basic building block of life here on Earth. Through their winds, they contribute ~85% of gas and ~35% of dust to the total enrichment of the interstellar medium (ISM; Tielens 2005) and are the dominant suppliers of pristine building blocks of interstellar material. The deterministic aspect seeks to answer the question of *how—how* and *how much* do cool aging stars contribute to the galactic chemical enrichment? Given some initial conditions at birth, in what way can evolved stars determine the evolution of a galaxy? Key questions include the following: which atoms are created and in what quantity? What are the mechanisms that transport the newly created elements from the core to the outer atmosphere? Which conditions can lead to the formation of molecules and solid-state dust species? Under which circumstances can a stellar wind form, and what are their resulting wind velocities and mass-loss rates?

The conceptual aspect addresses the more general and overarching question of *why—why* do cool aging stars contribute to the galactic chemical enrichment? This question is posed in the

Low- and intermediate-mass stars: stars that have an initial mass in the range of ∼0.8–8 M$_\odot$ and end their lives as white dwarfs if single

Interstellar medium: matter and radiation that exist between the stars in a galaxy

Stellar wind: flow of gas (and dust) particles ejected from the upper atmosphere of a star

sense of identifying the general physical and chemical laws, and their interactions. These laws are applicable not only to cool aging stars but to all of astrophysics. We are convinced, of course, that the laws of physics and chemistry are universal laws, but we must also admit that our knowledge of chemical processes is still very Earth-centric. As I discuss below, cool aging stars are unique laboratories that offer the exquisite possibility of teaching us about extraterrestrial and, hence, universal chemistry. The *how* and *why* questions inform one another and are interrelated. Ideally, we want to optimize our insight from both the deterministic and conceptual perspectives to obtain as complete a picture as possible of the late stages of stellar evolution.

Understanding the crucial role of cool aging stars, the asymptotic giant branch (AGB) stars and their more massive counterparts the red supergiant (RSG) stars, at the level of the conceptual framework requires further explanation. Although not always recognized, these stars deserve this critical status exactly because they are thought to be simple. Since the first identification of high-luminosity stars by Maury in 1897, their subsequent classification as giant stars by Hertzsprung (somewhere between 1905 and 1911), and the first solid evidence of matter escaping from a red giant star by Deutsch in 1956, their atmospheric and wind structures were thought to have an overall spherical symmetry, and hence they are described by one-dimensional (1D) equations. A large variety of chemical reactions occur in their wind, including unimolecular two- and three-body reactions, cluster growth, and grain formation. To date, more than 100 different molecules, and their isotopologues, and ~15 different solid-state species have been detected. The simple thermodynamical structure and chemically rich environment make these stars ideal candidates for disentangling the physical and chemical processes and unraveling the general laws governing not only these stars and their winds but also those in other chemically rich astrophysical environments, including high-mass star-forming regions, young stellar objects, protoplanetary disks, exoplanets, novae, SNe, and interstellar shocks.

However, recent findings complicate this picture. As I discuss below, the conceptual argument still remains valid, but its underlying reasoning gets sharpened while essential aspects deeply grounded in the deterministic question will encounter a reformulation. Ground-breaking observations, theoretical insights, numerical simulations, and laboratory experiments bear ample evidence that our notion of spherical stars and winds was oversimplified. The cool aging stars, which are the focus of this review, have an incredibly fascinating life and harbor 3D complexities that bridge 23 orders of magnitude in scale, from the nanometer up to thousands of astronomical units. The 3D life of molecules and solid-state aggregates, the emergence of 3D clumps, and the lasting 3D impact of a (hidden) companion offer challenges against which our physical knowledge and chemical understanding need to be reevaluated. Like Daedalus,[1] these stars are a symbol of wisdom, knowledge, and power; fortunately, the challenge that they pose is not a Gordian knot,[2] but it can be taken up successfully through an intensive collaboration with and access to modern observatories, state-of-the-art theoretical models, laboratory experiments, and high-performance computation (HPC) facilities. Only then will it be possible to better quantify the deterministic aspects of cool aging stars in the cosmological context and to have a more coherent picture of these stars for the conceptual framework.

2. SETTING THE STAGE: THE ONE-DIMENSIONAL WORLD

Quantifying the contribution of the cool evolved AGB and RSG stars to the chemical enrichment of our Universe implies that we need to know the absolute rate at which these stars eject matter

Asymptotic giant branch (AGB) stars: cool luminous stars that represent the late evolutionary stages of low- to intermediate-mass stars and exhibit strong stellar winds

Red supergiant (RSG) stars: cool massive stars that evolve from stars with initial mass of 10–30 $M_\odot$ and develop powerful stellar winds

Isotopologues: molecules that differ only in their isotopic composition

---

[1]Daedalus was a craftsman and artist in Greek mythology and the father of Icarus. He built the paradigmatic Labyrinth for King Minos of Crete and is seen as a symbol of wisdom, knowledge, and power.
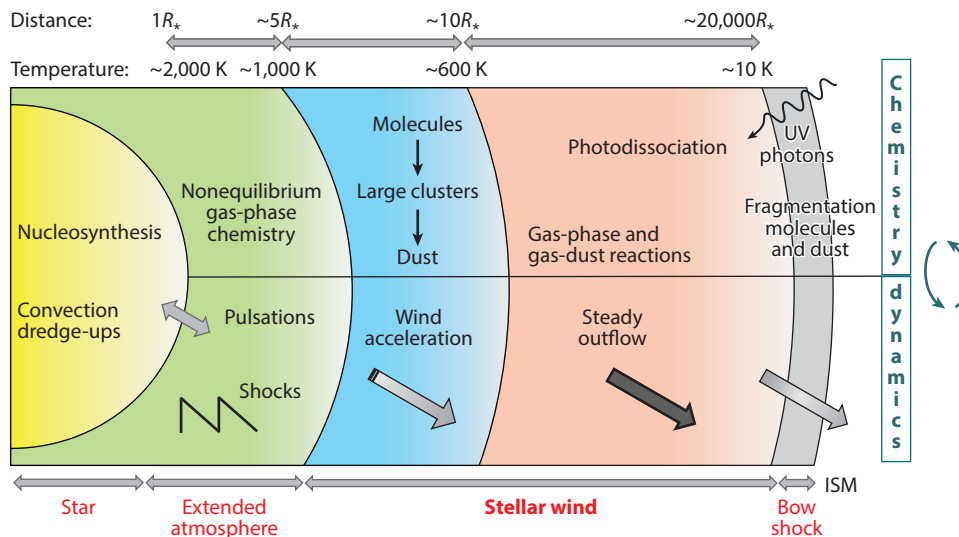[2]A Gordian knot is a metaphor for an intractable problem.

Figure 1

Schematic representation of an evolved AGB star and its circumstellar environment assuming spherical symmetry. The upper part illustrates the dominant chemical processes on length scales of nanometers to micrometers. The bottom part delineates the dynamical behavior acting on scales of astronomical units. Physical and chemical processes are closely interrelated, including an intense interaction with the radiation field. Typical radial distances and temperatures are indicated at the top of the figure, where the stellar radius, $R_\star$, is of the order of ~1 AU. Abbreviations: AGB, asymptotic giant branch; ISM, interstellar medium; UV, ultraviolet.

into the ISM—the mass-loss rate as a function of time, $\dot{M}(t)$—and the relative fraction of atoms, molecules, and solid dust species in their stellar wind as functions of radial distance, r, and time, t. It was not until the mid-1970s that estimates of the mass-loss rate were within reach and Goldreich & Scoville presented the first detailed thermodynamical model of a circumstellar envelope (CSE; see **Figure 1**) after the initial detections of circumstellar molecular line emission a few years earlier (Goldreich & Scoville 1976). Some brief historical reminders of this enlightening period are presented in Section 2.1. Beginning with their seminal work, I introduce the reader to some basic theoretical ingredients of stellar wind physics in Section 2.2. In that section, I mainly focus on the one crucial parameter of stellar evolution, which I foresee will experience major improvements in the next couple of years: the mass-loss rate during the end-phases of stellar evolution. Granted, our understanding of the relative contributions of atoms, molecules, and dust grains will see some major breakthroughs, but for the reasons I describe below, I think that a quantitative understanding of these will take at least a decade.

Circumstellar envelope (CSE): the region surrounding the star, encompassing the extended atmosphere, the stellar wind, and the bow shock

2.1. Bits of History

The first theoretical study of dust condensation in cool stars was performed by Wildt (1933). Using thermochemical calculations, Wildt considered the possibility that dust may contribute to the opacity in cool stellar atmospheres and showed that some very refractory solid compounds, i.e., refractory material, could be formed. But it took three decades until the far-reaching consequences of this work were realized. Motivated by the problem of identifying the origin of interstellar dust, Hoyle & Wickramasinghe (1962) suggested that graphite grains can condense in carbon-rich cool stars and can then be driven out by radiation pressure. (See the sidebar titled Carbon- and

CARBON- AND OXYGEN-RICH COOL STARS

For stars in the early AGB or RSG phase, the chemical abundances reflect the chemical composition of the matter from which the star was formed. The galactic carbon-to-oxygen abundance ratio, C/O, is generally lower than 1, with C/O ∼ 0.56 in the solar vicinity and attaining lower values for lower metallicities (Chiappini et al. 2003, Akerman et al. 2004). This implies that at the start of the AGB or RSG phase, stars are still oxygen-rich (O-rich, C/O < 1) and are categorized as M-type stars. During the AGB and RSG phase, carbon is fused in the stellar core owing to the triple-α process and is brought to the surface by convection. For AGB stars with an initial mass in the range of ∼1.5–4 $M_\odot$ (Straniero et al. 1997), the C/O ratio eventually becomes larger than 1, leading to a carbon star. Due to the exceptionally high C–O bond dissociation energy in CO, the less abundant of the two atoms (C or O) is completely bound in CO and cannot partake in the formation of solids (Gilman 1969) and other molecules. However, recent observations have challenged this idea: Molecules such as CO_2, CS, and HCN are detected in O-rich winds, and H_2O and SiO are detected in C-rich winds (see Section 5.1).

Oxygen-Rich Cool Stars.) Meanwhile, Deutsch (1956) provided the first evidence that matter is escaping from the RSG star α Her: Matter is flowing beyond the orbit of its G star companion at a speed of ∼10 km s^{-1}, which is well above the escape velocity at that distance. The estimated mass-loss rate was around 3×10^{-8} solar masses per year ($M_\odot$ year^{-1}). Parker described and solved the momentum equation (see Section 2.2) for the solar wind in 1958 and introduced the term stellar wind in 1960 (Parker 1958, 1960). Meanwhile, the ejection of matter was also detected for other red giants, such as the RSG star Betelgeuse (Weymann 1962b). The difficulty was explaining the apparently constant outflow of matter beyond 10 stellar radii with a speed of ∼10 km s^{-1}, which is less than the escape velocity from the star (Weymann 1962a). Wickramasinghe et al. (1966) were the first to propose that radiation pressure on grains can push the grains and the gas out of the stellar gravitational potential owing to momentum exchange between the dust and the gas.

Direct evidence of late-type stars with wind mass-loss rates well above a few 10^{-8} $M_\odot$ year^{-1} came to light at the end of the 1960s, but before that several indirect arguments were put forward to prove that stars must lose a significant fraction of their mass during the final evolutionary phases. One such argument came from Auer & Woolf (1965), who found that the Hyades cluster contains about a dozen white dwarfs; each should have a mass below the Chandrasekhar limit of 1.4 $M_\odot$. But the Hyades cluster is a young group, and stars with a mass of 2 $M_\odot$ are still on the main sequence. Hence, the white dwarf progenitors must have lost at least 0.6 $M_\odot$ during the post-main sequence phase, but they had not been observed at that time.

Ultimately, these mass-losing stars were detected in the late 1960s with the birth of infrared (IR) astronomy. Late M-type red giants were shown to often have an excess emission in the IR, an effect that was attributed to circumstellar dust. In 1968–1969 Gillett et al. (1968) and Woolf & Ney (1969) identified silicate grains in oxygen-rich AGB and RSG stars. Gehrz & Woolf (1971) derived the dust mass around a number of M-type stars, and using the expansion velocity from Deutsch, mass-loss rates in the range of 10^{-7}–10^{-5} $M_\odot$ year^{-1} were obtained. The first circumstellar molecular rotational transition detected at radio wavelengths was the OH maser (microwave amplification by stimulated emission of radiation) line at 1612 MHz toward the RSG NML Cyg (Wilson & Barrett 1968); the first thermally excited line was the CO $v = 0$, $J = 1$–0 transition detected a few years later toward the carbon star CW Leo (Solomon et al. 1971).

Using observations of similar RSG binary systems as Deutsch, Reimers (1975) was the first to derive an empirical mass-loss rate relation of the form

$$\dot{M} = 4 \times 10^{-13} \eta L/gR, \qquad\qquad 1.$$

Late-type stars: terminology used to indicate stars that are cool, here of spectral types K and M

The mass of the convective envelope decreases in time owing to both the stellar wind and nuclear burning ($4\,^1\mathrm{H} \rightarrow 1\,^4\mathrm{He}$), the latter effect resulting in an increase in core mass and, hence, luminosity (the Paczyński relation; Paczyński 1970). The difference in mass between the four fusing hydrogen nuclei and the newly created helium nucleus is converted to energy according to Einstein's equation $E = mc^2$ (Einstein 1905). The energy production per gram by H-burning, E_H, is 6.45×10^{18} erg g^{-1}. It follows that the nuclear burning rate, $\dot{M}_\mathrm{c}$, is given by $\dot{M}_\mathrm{c} = L_\star/E_\mathrm{H} = 1.02 \times 10^{-11}\, L_\star/L_\odot$ (in M$_\odot$ year^{-1}). For wind mass-loss rates above the nuclear burning rate, the associated timescale for stars to shed their envelope by a stellar wind is shorter than the nuclear burning timescale, such that mass loss determines the further evolution. Some authors denote this transition, occurring at a wind mass-loss rate of a few 10^{-7} M$_\odot$ year^{-1} (see Section 2.2.4), as the superwind phase (Lagadec & Zijlstra 2008, Zijlstra et al. 2009). However, we opt here to use the historical terminology of the word superwind, as first expressed by Renzini (1981), to indicate a mass-loss rate that greatly exceeds that prescribed by Reimers' law (see Equation 1; Reimers 1975). We recently argued that the maximum mass-loss rate during the superwind phase is a few 10^{-5} M$_\odot$ year^{-1} and, hence, is around the single-scattering radiation pressure limit, indicating that the ratio of the wind momentum per second, $\dot{M}v_\infty$, to the photospheric radiation momentum, $L_\star/c$, is around 1 (Decin et al. 2019).

with $\dot{M}$ the mass-loss rate in units of M$_\odot$ year^{-1}, η a unitless parameter of the order of unity, and the stellar luminosity L, gravity g, and radius R in solar units. For $\eta \sim 1$, the AGB lifetime is of the order of one million years, and the maximum AGB mass-loss rate is a few 10^{-6} M$_\odot$ year^{-1} (Renzini 1981). Renzini argued that a Reimers-like wind cannot explain the characteristics of planetary nebulae (PNe)—the descendants of the AGB stars—and he suggested the existence of a superwind developing at the high-luminosity tip of the AGB phase and with a mass-loss rate of at least a few 10^{-5} M$_\odot$ year^{-1} (Renzini 1981). (See the sidebar titled Superwind.) In the same year, Glass & Evans (1981) established the first linear relation between the K-band magnitude and the logarithm of the period in regularly pulsating Mira-type AGB variables. (See the sidebar titled Variability and Pulsation Modes.) Pulsations are thought to be an essential ingredient for the wind driving in AGB stars: Matter is levitated by shock waves induced by pulsations resulting in densities that are high enough at a few stellar radii for dust to condense and, in sufficient momentum, coupling between the gas and the grains. Observations indicate that the wind mass-loss rate ranges around $\sim 10^{-8}$–10^{-4} M$_\odot$ year^{-1} and the expansion velocity at $\sim$5–30 km s^{-1}. The discussions that took place during that period had a considerable impact on the field of stellar evolution modeling: In all calculations before, say, 1980 the assumption was made that the mass of a star did not change either by mass loss or mass accretion. Because the mass is the prime parameter determining the evolution and lifetime of a star, any modification to the stellar mass over time has large repercussions on its evolutionary path. A proper understanding of stellar evolution can thus not be achieved without a detailed understanding of wind mass-loss rates and, hence, wind physics.

Planetary nebula (PNe): short ($\sim 10^4$ years) evolutionary phase between the AGB and white dwarf phases, characterized by a hot central star that ionizes the gas ejected during the previous giant phase

2.2. Stellar Wind Physics

A central goal of stellar wind research is to derive a relation between the mass-loss rate and fundamental stellar parameters, such as the Reimers' relation (see Equation 1). Here, I wish to address a fundamental issue in the inductive method used to derive that relation—i.e., the issue of forward versus retrieval approaches. The forward method tends more toward the reductionist approach in the sense that one tries to understand phenomena in terms of the interaction of the constituent parts, whereas the retrieval method is more inclined toward the detection of (unexpected) emergent properties and, hence, can be argued to be more holistic in its approach, i.e., the

VARIABILITY AND PULSATION MODES

Variability in brightness is a common feature of AGB stars and is mainly caused by pulsations. The classification of pulsating AGB stars into Miras, Semiregulars (SR), and Irregulars was originally based solely on the appearance of light curves, without an understanding of the physical process at work. Mira variables have regular, large amplitude variations (variation in the visible light $\delta V > 2.5$ mag); semiregular variables are of smaller amplitude ($\delta V < 2.5$ mag) with some periodicity; and irregular variables show little periodicity although this is often due to a lack of detailed light curves. It turned out to be possible to trace the properties of variable stars through the period–luminosity (P–L) diagram, in which stars form distinct sequences depending on the pulsation mode responsible for their variability (Wood et al. 1999; see McDonald & Trabucchi 2019, their figure 1). Pulsating stars are often multiperiodic, and normally only the period with the largest amplitude is used in the P–L diagram. Mira variables are generally located on sequence C, which is due to pulsations in the fundamental mode. Sequences B and C′ are due to pulsation in the first overtone mode, and sequences A and A′ to pulsation in the second and third overtone modes, respectively. Sequences D and E are, respectively, due to long secondary periods and binary stars (Wood 2015). The semiregular variables occupy sequence A and B and the lower half of sequence C.

The energy transport, which determines the stability and growth rates of pulsation, is dominated by convection. Excitation of the pulsation modes in linear, nonadiabatic 1D models occurs through the H and first He ionization zones (the κ-mechanism). Most of the layers below the top of the H ionization zone with a temperature of $\sim$8,000 K contribute to the determination of the period of the fundamental mode, whereas all layers (including the surface layers) contribute in determining the higher overtones modes (Fox & Wood 1982). As a star evolves on the AGB, it rises on the P–L diagram and traverses the P–L sequences from left to right: Specific overtone modes gradually become stable, and the primary mode shifts toward lower radial orders (Trabucchi et al. 2019; see **Figure 2**).

whole is more than the sum of its parts. Both approaches are not mutually exclusive; rather, they inform each other. Let me briefly describe these approaches, in both their benefits and apparent shortcomings.

The forward approach is more mathematically oriented in that one seeks to describe all explicit and implicit relations between the quantities involved in a mathematically and physically consistent way. A self-consistent approach is even more restrictive and implies that all explicit input functions are the result of solving the system of basic equations of the problem, without introducing ad hoc assumptions. Resorting to these theoretically predicted mass-loss rates has the advantage of making the explicit dependence on individual input parameters studiable. However, the predictive power of any theoretical model is dictated by the level of description of the physical and chemical processes, and their interaction. In general, any realistic model should account for the thermodynamics, the hydrodynamics, the radiative transfer, and the chemistry including gas-phase and solid-state species; see **Figure 3**. Their combined action determines the local and global physical and chemical properties of the wind and, hence, the mass-loss rate. Various interactions shown in **Figure 3** are highly nonlinear with regard to both the chemical and physical description and the mathematical and numerical treatment. The forward approach can be highly demanding for the central processing unit (CPU) and, hence, a bottleneck for analyzing large samples of observational data.

To model observed quantities, one often resorts to retrieval modeling. Retrieval modeling implies that one prescribes externally parameters that are basically internal parameters. These (often simplifying) parameterizations are informed by the outcome of detailed forward modeling, or by an astrophysical hypothesis informed by specific observations and their analyses. As I demonstrate in Section 2.2.2, the solution to the momentum equation is often simplified by
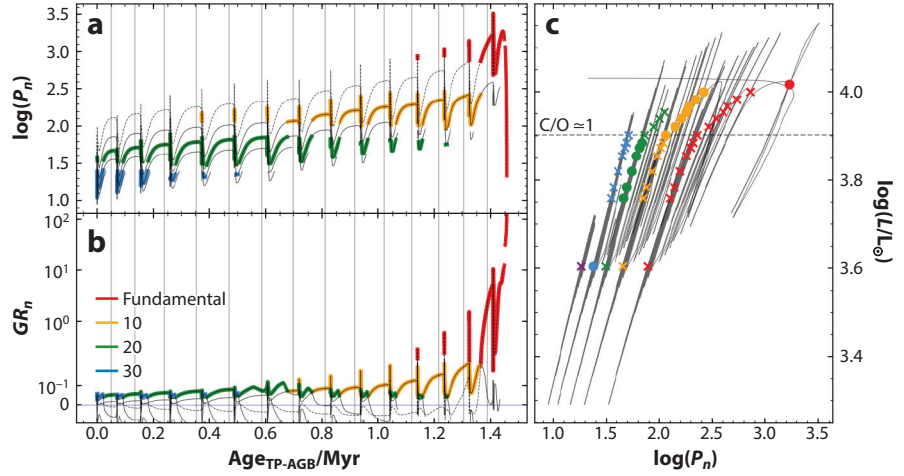
Figure 2

Pulsation periods, growth-rates, and period-luminosity diagram for a star evolving along the AGB phase. A linear, nonadiabatic 1D pulsation model is applied to an evolutionary track for a star with mass $M = 2.6\,M_\odot$ and metallicity $Z = 0.008$ at the beginning of the AGB phase. (*a*) Pulsation periods (in units of days) and (*b*) growth rates as a function of time elapsed since the beginning of the TP-AGB phase. Radial pulsation modes are identified by their radial order n, with $n = 0$ corresponding to the fundamental mode, $n = 1$ to the first overtone (1O) mode, $n = 2$ to the second overtone (2O) mode, and so on. For each mode n with eigenfrequency $\omega_n = \omega_{R,n} + i\omega_{I,n}$, the imaginary part of ω is the angular frequency of oscillation and the period of the nth mode is defined as $P_n = 2\pi/\omega_{I,n}$ with the amplitude growth rate calculated as $GR_n = \exp\left(2\pi \frac{\omega_{R,n}}{\omega_{I,n}}\right) - 1$. Dominant modes are highlighted by thick solid lines in colors. Modes other than the dominant are shown as thin solid lines, except for the fundamental mode, which is shown as dashed thin lines to be more easily distinguishable. Vertical lines mark the point of maximum luminosity of quiescent evolution at each thermal pulse cycle. As time elapses, the dominant mode gradually shifts toward lower radial orders. (*c*) Theoretical period-luminosity diagram. Symbols correspond to quiescent evolutionary points, with the dominant mode represented by a filled circle. The quiescent evolutionary points bend toward longer periods as the luminosity increases, especially for the fundamental mode, owing to the effect of mass loss. This bending is emphasized by the models transitioning to being carbon rich—indicated by the horizontal gray dashed line—which causes an increase of radius with respect to O-rich models at the same luminosity. Figure adapted with permission from Trabucchi et al. (2019). Abbreviations: AGB, asymptotic giant branch; TP-AGB, thermally pulsing AGB.

applying the β-velocity power law, and the solution to the energy equation by a temperature power law. The advent of new ground-based and space-borne missions has led to considerable progress in empirically derived mass-loss rate relations based on the use of retrieval methods. However, it turns out that these relations—which sometimes show dependencies on different fundamental parameters—are not always mutually consistent; see Section 2.2.4. The reasons for this discrepancy can be traced back to difficulties in determining highly accurate fundamental stellar parameters of AGB and RSG stars and the close entanglement of various of these parameters (such as luminosity, mass, age, and pulsation period). In addition, the parameterizations inherent in the retrieval method can yield a systematic bias in the derived mass-loss rates; systematic selection effects on observed samples might induce an unrecognized bias, and it is well established that correlation does not imply causality. I address some of these threats below.

The reductionist approach allows one to better demonstrate the various ingredients of stellar wind physics and chemistry. I therefore refer to that method in Section 2.2.1. As illustrated in **Figure 1**, the description of the CSE can be divided into three regions, and research groups tend to
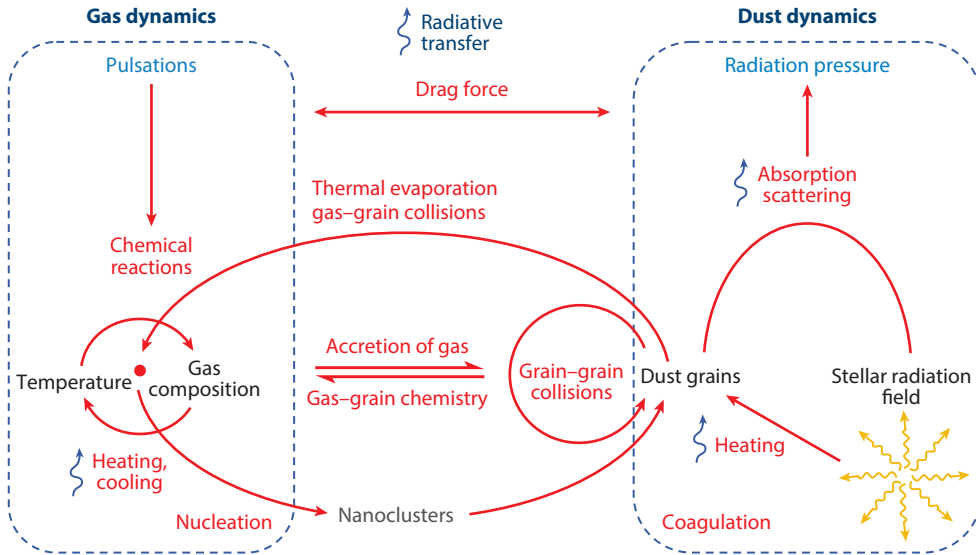
Figure 3

Schematic overview of the physical and chemical processes occurring in asymptotic giant branch winds. The two main driving forces are the pulsations of the star and the radiation pressure on dust grains. Both are self-consistently connected via the mechanisms depicted in the figure. Note that processes annotated with a curly blue arrow require the inclusion of radiative transfer calculations. Indicated in light blue are wind-driving forces, in black are physical and chemical quantities, in red are interactions, and in dark blue are different physics categories (dynamics and radiative transfer). Figure adapted from Boulangier (2019).

focus on the detailed description of one of them: (*a*) the extended atmosphere, in which pulsation-induced shocks result in a chemistry that is not in thermodynamic equilibrium (TE; e.g., Willacy & Cherchneff 1998, Cherchneff 2006, Gobrecht et al. 2016, Höfner & Olofsson 2018, Bladh et al. 2019); (*b*) the wind formation zone, in which radiation pressure on newly formed dust grain leads to the onset of the stellar wind, hence initiating the mass loss (e.g., Dominik et al. 1993, Gail & Sedlmayr 1999, Höfner & Olofsson 2018, Bladh et al. 2019); and (*c*) the steady outflow zone, in which the wind is freely expanding and is interacting with the surrounding interstellar radiation field resulting in photodissociation of molecules and further modification of the grain spectrum (e.g., Willacy & Millar 1997, Patzer 1998, Glassgold 1999, Agúndez et al. 2010, Li et al. 2014, Van de Sande et al. 2018b). Although time dependency is inherent in the description of region 1, the other two regions are often modeled using a stationary approach.

2.2.1. Standard circumstellar envelope model. For our discussion, it is sufficient to remind the reader of the general conservation laws describing the stellar wind structure under the assumption of (*a*) stationarity, because it allows us to obtain insight into the complex interplay between various physical and chemical processes, and (*b*) spherical symmetry (see Olofsson et al. 2010), because this is suggested by various observations of extended CSEs. In this situation, the hydrodynamics as expressed in the equations of mass and momentum conservation can be written as (e.g., Goldreich & Scoville 1976)

$$\frac{dM(r)}{dt} = \dot{M}(r) = 4\pi r^2 \rho(r) v(r), \qquad 2.$$

$$v(r)\frac{dv(r)}{dr} = [\Gamma(r) - 1]\frac{GM_\star}{r^2}, \qquad 3.$$

where $\dot{M}(r)$ refers to the mass-loss rate of the gas at a radial distance r from the star, $\rho(r)$ is the gas density, $v(r)$ is the gas velocity, $M_\star$ is the stellar mass, G is the gravitational constant, and $\Gamma(r)$ is the ratio of the radiation pressure force on the dust to the gravitational force, which can be written as (Decin et al. 2006)

$$\Gamma(r) = \frac{3v(r)}{16\pi \rho_s c G M_\star \dot{M}(r)} \iint \frac{Q_\lambda(a,r)L_\lambda \dot{M}_d(a,r)}{a[v(r) + v_{drift}(a,r)]}\, d\lambda\, da, \qquad 4.$$

with ρ_s the specific density of dust, c the speed of light, $\dot{M}_d$ the mass-loss rate of the dust, $v_{drift}(a,r)$ the drift velocity of a grain of size a, $Q_\lambda(a,r)$ the dust extinction efficiency, and L_λ the monochromatic stellar luminosity at wavelength λ.

From the first law of thermodynamics expressing the conservation of energy, the perfect gas law, and the equation of mass conservation, the thermal structure of the gas is governed by the relation (Goldreich & Scoville 1976)

$$\frac{1}{T(r)}\frac{dT(r)}{dr} = -\frac{4}{3r}\left[1 + \frac{1}{2}\frac{d\ln v(r)}{d\ln r}\right] + \frac{2}{3}\frac{H(r) - C(r)}{k\,T(r)\,v(r)\,n_{H_2}(r)\,[1 + f_H(r)]}, \qquad 5.$$

with $H(r)$ and $C(r)$ the total heating and cooling rate per unit volume, respectively; $n_{H_2}(r)$ the number density of H_2; and $f_H(r)$ the number fraction of atomic to molecular hydrogen. The first term on the right-hand side of Equation 5 represents the cooling due to adiabatic expansion in the case of constant mass loss. The second term, which represents the balance of the heating- and collision-driven radiative cooling processes, needs a proper treatment of the radiative transfer and the radial abundance profile of molecules such as H_2, H_2O, CO, and HCN and of the grains to calculate $C(r)$ and $H(r)$; see, for example, Decin et al. (2010).

The balance of radiative energy gain and radiative energy loss is used to calculate the temperature of an individual grain of dust, T_d,

$$\int_0^\infty \sigma_{d,\nu}^{abs} \left\{ J_\nu(r) - B_\nu[T_d(a,r)] \right\} d\nu = 0, \qquad 6.$$

with $\sigma_{d,\nu}^{abs}$ the absorption opacity of the dust grain at frequency ν, $J_\nu(r)$ the local mean radiation intensity, and B_ν the Planck function. At temperatures higher than the condensation temperature, the grain will sublimate.

For the purpose of radiation hydrodynamics (RHD), the treatment of the radiative transfer is often simplified. A well-known method has been proposed by Mihalas & Hummer (1974) and is based on the zero- and first-order moment transport equations,

$$\frac{dH_\nu(\tau_\nu)}{d\tau_\nu} = J_\nu(\tau_\nu) - S_\nu(\tau_\nu), \qquad 7.$$

$$\frac{dK_\nu(\tau_\nu)}{d\tau_\nu} = H_\nu(\tau_\nu), \qquad 8.$$

with τ_ν the optical depth, S_ν the source function, H_ν the flux, and K_ν being related to the radiation pressure $p_\nu = (4\pi/c)K_\nu$. Equations 7 and 8 make up a system of coupled integro-differential equations that can be mathematically closed by defining the Eddington factor,

$$f_\nu(r) = \frac{K_\nu(r)}{J_\nu(r)}, \qquad 9.$$

with $f_\nu(r)$ approaching 1/3 for an isotropic radiation field.

The chemical evolution of the composition of a closed system is dictated by a set of chemical formation and destruction reactions. Mathematically, this is a set of coupled ordinary differential equations in which the change in number density of the ith species is given by

$$\frac{\mathrm{d}n_i}{\mathrm{d}t} = \sum_{j \in F_i} \left(k_j \prod_{r \in R_j} n_r \right) - \sum_{j \in D_i} \left(k_j \prod_{r \in R_j} n_r \right).$$

10.

The first term, within the summation, represents the rate of formation of the ith species by a single reaction j of a set of formation reactions F_i. The second term is the analog for a set of destruction reactions D_i. Each reaction j has a set of reactants R_j, where n_r is the number density of each reactant and k_j the rate coefficient of this reaction. For chemistry in TE, Equation 10, involving both gaseous and dust species, reduces to the well-known law of mass action (Gail & Sedlmayr 2013),

$$\prod_{\substack{i \\ \text{all gases}}} \left(\frac{p_i}{p_0} \right)^{v_i} \prod_{\substack{i \\ \text{all solids}}} \left(a_i^c \right)^{v_i} = e^{-\Delta G / RT},$$

11.

with v_i the stoichiometric coefficients, the activity a_i^c of species i defined as $a_i^c = p_i / p$, p the pressure, p_i the partial pressure of species i, p_0 the standard pressure of 1 bar, R the gas constant in units as used for the data of ΔG, and G the Gibbs function, so that

$$\Delta G = \sum_i v_i G_i(p_0, T),$$

12.

with $G_i(p, T)$ being the partial free enthalpy of 1 mole of species i at temperature T and pressure p. Chemical equilibrium (CE) is established if the chemical reaction timescales are small compared to other competing timescales governing the considered concentrations, so that Equation 11 is only dependent on temperature.

Together with suitable boundary and initial conditions, the resulting mathematical system $\mathcal{M}$ described in Equations 2 and 12 constitutes a complete and well-posed set of coupled equations given a set of independent fundamental stellar parameters. The solution provides a theoretical prediction of the physical and chemical quantities, including the mass-loss rate and the spectral appearance. By choosing the stellar mass, temperature, luminosity, and abundance composition $\{M_\star, T_\star, L_\star, \{\epsilon_X\}\}$ as independent stellar parameters, we can express this formally as (Gail & Sedlmayr 2013)

$$\{M_\star, T_\star, L_\star, \{\epsilon_X\}\} \stackrel{\mathcal{M}}{\Longrightarrow} \dot{M}.$$

13.

Admittedly, the chemical abundances $\{\epsilon_X\}$ are genuinely free parameters only for stars in the early AGB phase. In principle, the elemental abundances result from stellar evolution—i.e., in particular, nucleosynthesis and convection-induced dredge-up processes—so the stellar mass and chemical abundances are not independent. However, the timescales involved with stellar evolution are much larger than those of the physical and chemical processes considered here. This implies that mass and chemical abundances only vary on secular timescales and can be considered as independent stellar parameters.

2.2.2. Outcome of stationary one-dimensional model predictions.
Given the assumption of stationarity, any model prediction applies for a genuinely dust-driven wind; but see Section 2.2.3. The radial structure for a low-mass carbon-rich star at the tip of the AGB phase is shown in **Figure 4**. Efficient dust nucleation around 3 stellar radii enables a dust-driven wind. The gas pressure, and hence also the density ρ, decreases approximately exponentially near the photosphere, with $\rho \propto r^{-2}$ further out due to the condition of mass conservation. The gas expansion
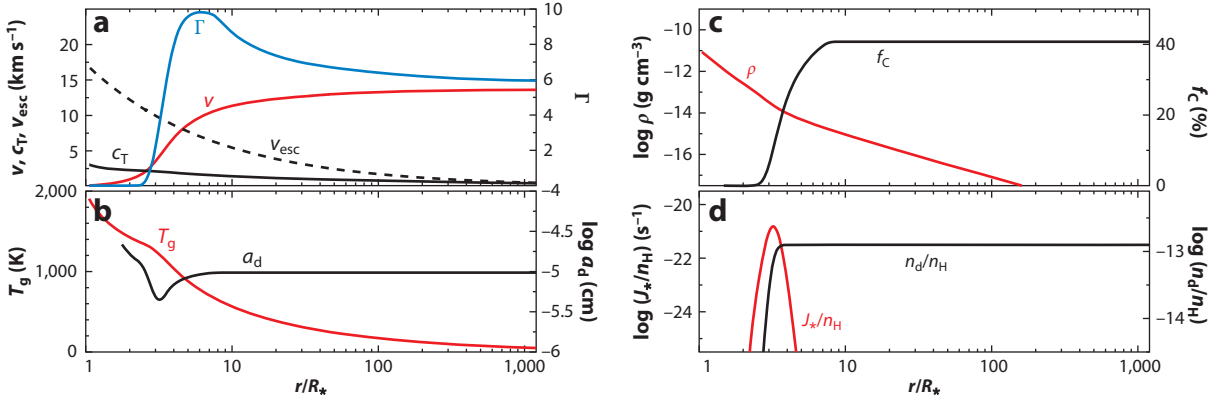
Figure 4

Radial structure for a stationary dust-driven wind with independent fundamental parameters $M_\star = 0.7\ M_\odot$, $L_\star = 2.4 \times 10^4\ L_\odot$, $\dot{M} = 8 \times 10^{-5}\ M_\odot$ year^{-1}, $\{\epsilon_{X \neq C}\}_\odot$, and $\epsilon_C/\epsilon_O = 1.4$ and assuming homogeneous nucleation with C_1 as basic monomer. (*a*) Gas velocity v, isothermal sound speed c_T, escape velocity v_{esc}, and radiative acceleration in units of the gravitational acceleration Γ; (*b*) radiative equilibrium gas temperature T_g and dust grain size a_d; (*c*) mass density ρ and degree of condensation, that is, the fraction f_c of the amount of carbon condensate relative to the condensable carbon present in the gas phase; (*d*) nucleation rate $J_\star$ and grain particle density n_d, with both quantities normalized to the number density of hydrogen nuclei n_H. The nucleation rate $J_\star$ corresponds to the formation rate of the gas-phase cluster that is the least abundant and, hence, will dictate the dust formation rate; see Section 5.3. Figure courtesy of H.-P. Gail.

velocity, v, exceeds the local escape velocity, v_{esc}, at around 3 stellar radii and the wind becomes gravitationally unbound, reaching a terminal wind velocity, v_∞, of around 22 km s^{-1}. In retrieval modeling, this particular behavior of the wind acceleration is often approximated by the so-called β-type velocity law (Lamers & Cassinelli 1999):

$$v(r) = v_0 + (v_\infty - v_0)\left(1 - \frac{R_{dust}}{r}\right)^\beta,\qquad 14.$$

with r the distance to the star and v_0 the velocity at the dust condensation radius R_{dust}. Low values for β describe a situation with a high wind acceleration value. In the same vein, the gas and dust temperature structure are often approximated by a power law,

$$T(r) = T_\star \left(\frac{R_\star}{r}\right)^\zeta,\qquad 15.$$

with $\zeta \approx 0.5$–0.6.

Stationary wind models typically predict terminal wind velocities in the range of 5–20 km s^{-1}, and mass-loss rates in the range of $\sim 5 \times 10^{-8} - 3 \times 10^{-4}\ M_\odot$ year^{-1} for carbon-rich winds, where the maximum mass-loss rate is a factor of a few lower for oxygen-rich winds (De Beck et al. 2010, Gail & Sedlmayr 2013, Decin et al. 2019). A higher luminosity and lower temperature induce higher mass-loss rates and expansion velocities due to the larger radiation pressure on the dust grains and the potential for more efficient dust nucleation and growth, respectively. The mass-loss rate is very sensitive to the stellar mass via its effect on the gravity and, hence, $\Gamma(r)$: a reduction of the stellar mass by a factor of 2 leads to an increase of the mass-loss rate by a factor 3 to 100 (Gail & Sedlmayr 2013). This effect might thus be a natural candidate to explain the superwind scenario proposed by Renzini (1981), because the AGB stellar mass will be reduced significantly by the preceding mass loss.

For RSG stars the role of grains close to the star remains unresolved, and radiation pressure on molecular lines, turbulent pressure, acoustic waves, and Alfvén waves (Alfvén 1942) have been

Dust condensation radius (R_{dust}): radial distance at which the first solid-state species are formed

Turbulent pressure: pressure caused by small-scale motions of stochastic nature

Acoustic wave: mechanical and longitudinal wave resulting from 3D fluctuations in the pressure field

Alfvén wave: a transverse electromagnetic wave propagating along the magnetic field lines of a plasma

VARIABILITY AND MASS-LOSS RATES

For Mira-type variable stars with a luminosity above ~2,000 $L_\odot$ and pulsation period P of ~300–800 days, a linear relation exists between the period and the logarithm of the mass-loss rate (~10^{-7} $M_\odot$ year^{-1} < $\dot{M}$ < 3 × 10^{-5} $M_\odot$ year^{-1}), suggesting that the corresponding increase in luminosity causes the radiation pressure on dust to be more effective. Semiregular variables with $P \lesssim 200$ days cover essentially the same mass-loss rate regime as the Mira variables with a period of 200–400 days, whereas a maximum mass-loss rate of a few 10^{-5} $M_\odot$ year^{-1} seems to be reached for $P \gtrsim 800$ days (Vassiliadis & Wood 1993, De Beck et al. 2010). Between ~60 and ~300 days, an approximately constant mass-loss rate of ~3.7 × 10^{-7} $M_\odot$ year^{-1} is found, whereas for $P < 60$ days the mass-loss rate is a factor of ~10 smaller. This rapid increase of mass-loss rate and dust production when the star first reaches a pulsation period of ~60 days coincides approximately with the point when the star transitions to the first overtone pulsation mode, whereas the second rapid mass-loss rate enhancement at $P \sim 300$ days coincides with the transition to the fundamental pulsation mode. This indicates that stellar pulsations are the main trigger for the onset of the AGB mass loss and are significant in controlling the mass-loss rate (McDonald & Zijlstra 2016, McDonald & Trabucchi 2019).

proposed as alternative mechanisms (Josselin & Plez 2007, Bennett 2010, Scicluna et al. 2015, Montargès et al. 2019, Kee et al. 2021). In general, these alternative processes might also support the AGB stellar wind, although their role in driving the wind is very much debated (Wood 1990, Gustafsson & Höfner 2003).

2.2.3. Limitations of the stationary approach. The standard 1D CSE description (Section 2.2.1) is time independent and, hence, does not treat the extended atmosphere in which pulsations induce shock waves that levitate the gas to distances at which dust can form. It is generally accepted that pulsations are a key ingredient of AGB mass loss (Bowen 1988, McDonald & Zijlstra 2016, McDonald & Trabucchi 2019; see the sidebar titled Variability and Mass-Loss Rates); however, the nature of the pulsations and their impact on the density scale height continues to be a source of debate. The stellar interior where these variations originate is an optically thick region dominated by convection that has proven difficult to model. Linear, nonadiabatic 1D pulsation models have been successful in predicting the overtone modes expected to occur in early-type AGB semiregular variables, but poor agreement is found for the fundamental mode Mira-type pulsators (Trabucchi et al. 2017, 2019).

A global 3D RHD approach targeted at the convection, and related pulsations, has recently been explored by Freytag et al. (2017). Due to computational constraints, the models only reach up to ~2 $R_\star$. Irregular structures with convection cells dominate in the interior part and propogate shocks in the outer atmosphere. The models develop radial pulsations and nonradial pulsations, but with a different frequency between the inner and outer parts of the model. For models in which the radial fundamental mode dominates, the pulsation periods range between ~300 and 630 days, in good agreement with observations for Mira-type variables. The exact mechanism for the mode excitation is, however, not yet fully understood, and possibilities such as stochastic excitation by convection, excitation by the κ-mechanism, and acoustic noise are explored by the authors.

Owing to the complex nature of pulsation, various researchers have treated their effects in a 1D parameterized way following the piston approach (Bowen 1988, Gauger et al. 1990, Höfner et al. 1995). These wind models typically have an inner boundary situated just below the photosphere of the star, where the radius and luminosity are assumed to have sinusoidal variations characterized by the pulsation period P and velocity amplitude Δv_p. The pulsation period can

Nonadiabatic:
occurring with loss or gain of heat or mass between the thermodynamic system and its surroundings

Radial pulsation:
occurs when a star oscillates around the equilibrium state by changing its radius symmetrically over the whole surface

Nonradial pulsation:
some parts of the stellar surface are moving inward, whereas others move outward at the same time

be derived from the period–luminosity (*P–L*) relation. The velocity amplitude, Δv_p, is typically in the range of 2–4 km s^{-1}, corresponding to shock amplitudes of $\sim$15–20 km s^{-1} in the inner atmosphere (Bladh et al. 2019). This standard inner boundary condition is meant to describe the pulsation properties of Mira variables pulsating in the fundamental mode, but a similar simplified approach for semiregular variables has not yet been pursued. Formally, we can express the 1D piston models as (Gail & Sedlmayr 2013)

$$\{M_\star, T_0, L_0, \{\epsilon_X\}, P, \Delta v_p\} \overset{\mathcal{M}}{\Longrightarrow} \dot{M}, \qquad 16.$$

with $T_0 = T_\star(t = 0)$ and $L_0 = L_\star(t = 0)$. The predicted wind velocities and mass-loss rates show no significant differences compared with more complex models in which (the mean of) the dynamical properties predicted by the 3D RHD models are used as inner boundary conditions for the dust-driven wind (Liljegren et al. 2018).

Using the piston approach, model grids for carbon- and oxygen-rich winds have been published by Arndt et al. (1997), Eriksson et al. (2014), and Bladh et al. (2019), respectively. The grid of 48 models by Arndt et al. (1997) self-consistently calculates the dust nucleation by assuming CE and homogeneous nucleation with C_1 as the basic monomer, whereas the more extensive grids of Eriksson et al. (2014) and Bladh et al. (2019) assume the presence of dust seeds, or seed particles, that can act as further building blocks for grain growth. More on these two different approaches can be found in Section 5. Arndt et al. (1997) have presented a linear multivariate regression analysis by means of a multidimensional maximum-likelihood method to derive an explicit mass-loss rate formula for the implicit mass-loss relation of pulsation-enhanced dust-driven winds, with a best-fit formula being

$$\log \dot{M}_{\mathrm{fit}} = -4.95 - 2.8 \log[M_\star(\mathrm{M}_\odot)] + 1.65 \log\left[\frac{L_0(\mathrm{L}_\odot)}{10^4}\right] - 9.45 \log\left[\frac{T_0(\mathrm{K})}{2{,}600}\right]$$
$$+ 0.470 \log\left(\frac{\epsilon_C/\epsilon_O}{1.8}\right) - 0.146 \log\left[\frac{P(\mathrm{days})}{650}\right] + 0.449 \log\left[\frac{\Delta v_p(\mathrm{km\,s}^{-1})}{2}\right], \qquad 17.$$

with $\dot{M}_{\mathrm{fit}}$ in units of M$_\odot$ year^{-1}. From the regression coefficients it is clear that $\dot{M}_{\mathrm{fit}}$ is strongly influenced by T_0, $M_\star$, and L_0 and is only weakly dependent on Δv_p, ϵ_C/ϵ_O, and P. This outcome renders the possibility of a reduced fit, with an equally high correlation coefficient,

$$\log \dot{M}_{\mathrm{fit}} = -4.93 - 2.88 \log[M_\star(\mathrm{M}_\odot)] + 1.53 \log\left[\frac{L_0(\mathrm{L}_\odot)}{10^4}\right] - 8.26 \log\left[\frac{T_0(\mathrm{K})}{2{,}600}\right]. \qquad 18.$$

The results published by Bladh et al. (2019) allow for a similar linear multivariate regression analysis, yielding

$$\log \dot{M}_{\mathrm{fit}} = -5.26 - 3.82 \log[M_\star(\mathrm{M}_\odot)] + 3.17 \log\left[\frac{L_\star(\mathrm{L}_\odot)}{10^4}\right] - 6.47 \log\left[\frac{T_{\mathrm{eff}}(\mathrm{K})}{2{,}600}\right]. \qquad 19.$$

Although Equations 17 and 18 refer to the temperature and luminosity at time $t = 0$ when the piston position takes its mean value over the pulsation period and is moving outward with maximum speed, Equation 19 uses the effective temperature and stellar luminosity of the hydrostatic dust-free model that was used as a starting structure for the calculations. Although any impact of the pulsation practically cancels in Equations 18 and 19, the pulsation quantities have an important implicit influence. The reason is that pulsations increase the density scale height, allowing for efficient condensation and growth of dust species. This outcome explains why an empirically derived mass-loss rate formula, such as the one proposed by Reimers, can be expressed in terms of fundamental stellar parameters without notion of the pulsation characteristics—for Reimers' law being $L_\star$, $R_\star$, and $M_\star$ (see Equation 1 in Section 2.1).

2.2.4. Theoretical versus empirical mass-loss rate relations. The similar dependence between the mass-loss rate and some of the fundamental stellar parameters identified by the forward and the retrieval approaches has nurtured the idea that empirically derived mass-loss rate relations could provide an alternative approach for understanding the essence, if not the detail, of the process by which mass loss occurs. The advent of new observing facilities resulted in tremendous progress in the field of observational astrophysics. Molecular lines and dust emission have been used to retrieve the mass-loss rate of the stars under study (Höfner & Olofsson 2018, and references therein). Circumstellar CO rotational and OH maser emission are the molecular diagnostics most often used to estimate the gas mass-loss rates (e.g., Baud & Habing 1983, Schöier et al. 2002, Decin et al. 2006, Ramstedt et al. 2008, De Beck et al. 2010). The benefit of analyzing molecular lines is that one obtains the expansion velocity. The disadvantages are that the observation of emission from thermally excited lines is typically limited to nearby stars within ∼2 kpc from the Sun (although the sensitivity of the Atacama Large Millimeter/submillimeter Array (ALMA) is now opening up the field to larger distances, such as the Large Magellanic Cloud; Groenewegen et al. 2016), the unknown fractional abundance of the molecule, and the fact that the analysis often requires a nonlocal thermodynamic equilibrium (non-LTE) radiative transfer analysis, which can be quite CPU intensive. The latter aspect implies that sample studies seldom exceed ∼50 stars (Danilovich et al. 2015), whereas the calculation of dust spectral features—and the related analysis of the spectral energy distribution (SED)—are readily applied to large samples, owing to the inherently simpler radiative transfer calculations. However, the identification of dust features is more ambiguous, and a reliable estimate of the mass-loss rate of the dust can only be achieved if several dust features with differing optical depths are combined. In addition, one needs to assume a dust expansion velocity and a gas-to-dust mass ratio to convert the derived dust densities into gas mass-loss rates (e.g., Heras & Hony 2005, Groenewegen et al. 2009, Verhoelst et al. 2009).

Supported by the incredible increase in computational power during the past two decades, a whole family of mass-loss rate relations has been derived. Without any attempt for completeness, I have summarized some of these theoretical, empirical, and semiempirical relations in the **Supplemental Text**, where I focus on those relations that have an explicit dependence on two of the main fundamental stellar parameters: the luminosity and the effective temperature. For an AGB star of stellar mass 2 $M_\odot$ or with an effective temperature of 2,800 K, these mass-loss rate relations are shown in **Figure 5a,b**; for an RSG star of mass 15 $M_\odot$ or with an effective temperature of 3,500 K, the mass-loss prescriptions are shown in **Figure 5c,d**; more detailed information is provided in the **Supplemental Text**. The large diversity between prescriptions is remarkable, with differences up to two orders of magnitude or higher. To be fair, not all mass-loss rate formulae are applicable to all classes of cool aging stars, so sometimes we might be comparing apples with oranges. But even within the class of the "apples," it seems that we are having different cultivars in the same basket; let's call them the medium-sized *Golden Russets*, which make extraordinary cider, and the large red-colored *Haralsons*, which are an excellent choice for pies. Both are different genomic expressions of the *malus pumila* and in the same vein the relations we witness in **Figure 5** are different expressions of an emergent property: the mass-loss rate. This statement deserves further explanation.

Indeed, while the various mass-loss rate proposals seem already disappointingly incompatible with huge differences, there is still another underlying conceptual complication. Given these differences, it is to be expected that the impact of a particular choice of mass-loss rate on stellar evolution calculations will be significant. This is illustrated in **Figure 6**, where a set of
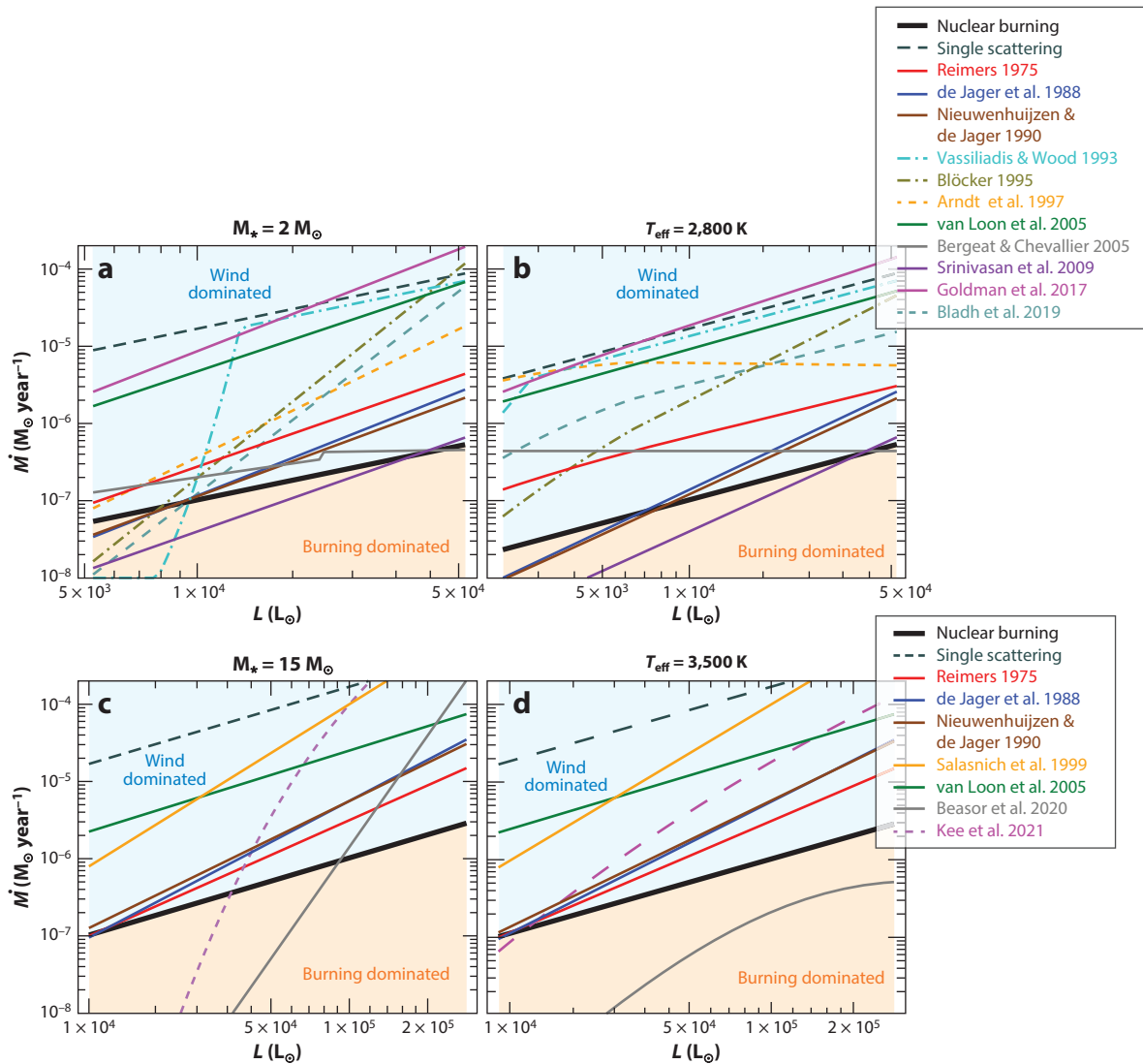
Figure 5

Mass-loss rate as a function of luminosity. The upper two panels show mass-loss rate prescriptions for AGB stars, at (*a*) a fixed stellar mass of 2 $M_\odot$ and (*b*) a fixed effective temperature of 2,800 K; the bottom two panels apply to RSG stars, at (*c*) a fixed stellar mass of 15 $M_\odot$ and (*d*) a fixed effective temperature of 3,500 K. Empirical mass-loss rate relations are displayed with a solid line, semiempirical relations with a dash-dotted line, and theoretical relations with a dashed line. The rate at which hydrogen is consumed by nuclear burning, $\dot{M}_c = 1.02 \times 10^{-11} L_\star$, is shown as thick black line; the single-scattering radiation pressure limit for an expansion velocity of 12 km s^{-1} is shown as dashed dark gray line. Stellar mass loss rules the evolution of the AGB and RSG stars if the wind mass-loss rate exceeds the nuclear burning rate, as indicated by the light-blue region; the hydrogen-burning dominated region is indicated by the light-orange region. The change in the slope for the Vassiliadis & Wood (1993) description is caused by the stellar mass exceeding the limit of 2.5 $M_\odot$ (see the **Supplemental Text, Equations S5 and S6**); the jump for the Bergeat & Chevallier (2005) description in the left panel is due to the effective temperature getting below 2,900 K (see the **Supplemental Text, Equations S15 and S16**). More detailed information is provided in the **Supplemental Text**. Abbreviations: AGB, asymptotic giant branch; RSG, red supergiant.
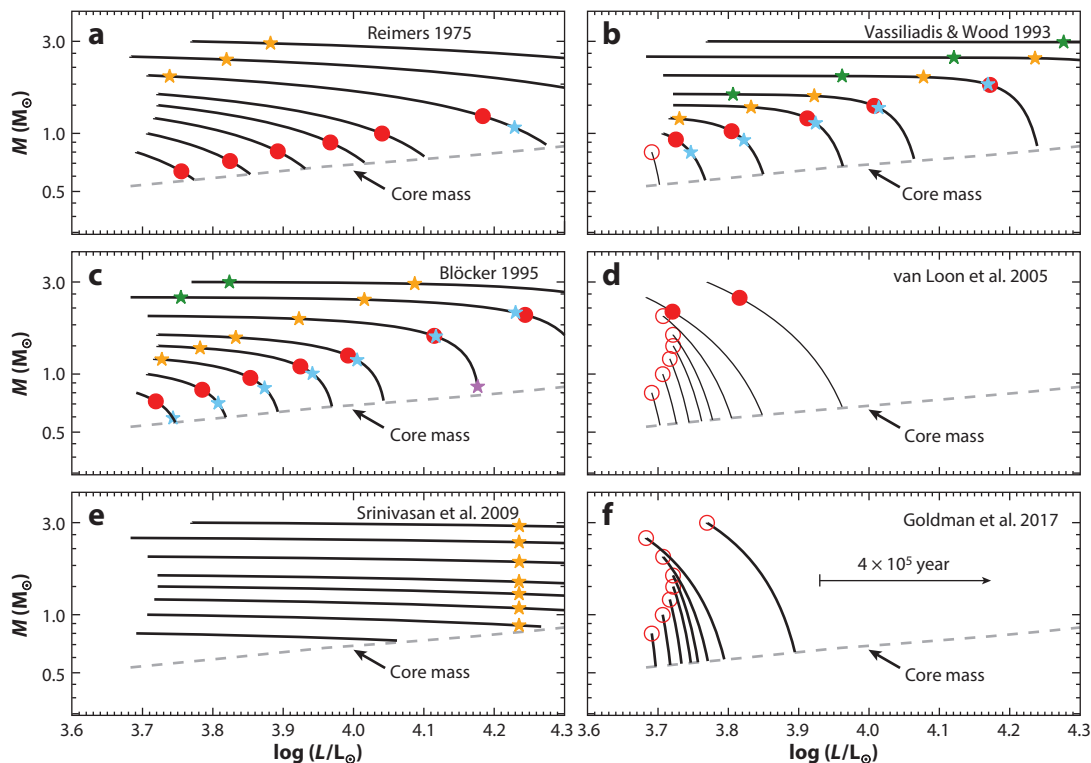
Supplemental Material >

Figure 6

Evolution in mass and luminosity for stars with a solar composition for different mass-loss rate prescriptions. The different tracks show the stellar evolution for AGB stars with a mass at the first thermal pulse of 0.8, 1.0, 1.2, 1.4, 1.6, 2.0, 2.5, and 3 $M_\odot$. In each panel, a different mass-loss rate prescription has been used, as indicated in the top right corner. The core–mass–luminosity relation is displayed by the dashed gray line. The filled red circles indicate the locus, where $d\log M_\star/dt = d\log L_\star/dt$; an open red circle implies $d\log M_\star/dt$ is larger than $d\log L_\star/dt$ at the start of the calculation. The colored stars specify the locus, where $\dot{M}$ is equal to 10^{-8} (*green*), 10^{-7} (*orange*), 10^{-6} (*cyan*), and 10^{-5} (*magenta*) $M_\odot$ year^{-1}. The rate of change of the star's abscissa in this plot is $d\log L_\star/dt = 0.605$ Myr^{-1}, which is indicated by the black arrow in panel *f*. Abbreviation: AGB, asymptotic giant branch.

simplified evolutionary tracks is shown for stars with an AGB mass at the first thermal pulse[3] in the range of 0.8–3 $M_\odot$ (see the **Supplemental Text** for more information). For the Blöcker (1995) and Vassiliadis & Wood (1993) mass-loss rate relations that have a strong dependence on luminosity, the stars evolve on a nearly horizontal track—where the mass remains approximately constant—until the star reaches the locus where $d\log M_\star/dt = d\log L_\star/dt$ (referred to as the cliff by Willson 2000, see **Figure 6**). For the set of models shown in **Figure 6**, the mass-loss rate at the cliff is around 0.5–1.7 × 10^{-6} $M_\odot$ year^{-1}. Passing beyond that implies that the evolution is further ruled by the wind mass-loss rate, which for the Blöcker (1995) and Vassiliadis & Wood (1993) relations implies an asymptotic downhill behavior. This particular behavior let Willson (2000) identify a strong selection effect concerning stars for which the mass-loss rate is measurable. Stars not yet near the cliff will have low mass-loss rates that are difficult to detect or measure, whereas stars beyond the cliff will be short-lived, causing a scarcity in the detection rates.

---

[3]A thermal pulse is caused by a helium shell flash, occurring over periods of 10,000 to 100,000 years, and lasting only a few hundred years.

This implies a selection bias toward stars near the cliff. Thus, the empirical mass-loss laws "tell us the parameters of the stars that are losing mass, and not the dependence of the mass-loss rates on the parameters of any individual star" (Willson 2000, p. 600). Although the 1-dex width in mass-loss rate around the cliff is not necessarily that narrow—all depend on the particular mass-loss rate behavior over time—Willson's conclusion remains valid: empirical mass-loss rate formulae "tell us which stars are losing mass rather than how stars are losing mass over time." (Willson 2000, p. 573)

This conclusion by Willson brings us back to the earlier discussion of the benefits (but also pitfalls) of the reductionist approach. At the risk of oversimplification, this approach is linked to that termed hierarchical reduction: the idea that phenomena at one hierarchical level can be explained by using concepts from a lower hierarchical level. Thus, we conventionally express astrophysical phenomena in terms of chemical principles, and chemical phenomena in physical terms, and physical phenomena in a mathematical language; or as the Nobel Prize–winning physicist Steven Weinberg succinctly expressed that explanatory arrows always point downward (Weinberg 1994). Empirical mass-loss rate prescriptions do not follow the arrow downward, but are holistic expressions of an emergent property and, hence, take a top-down approach in their attempt to unravel stellar evolution. Indeed, quite confusingly, top-down does not imply point downward in Weinberg's words. The risk of an emergent property is that it raises the expectation that the behavior is understood, but that is not necessarily true. In this particular case, I would not recommend using empirical mass-loss rate relations in stellar evolution models, because the seemingly logical relation might be causally wrong. In contrast the forward theoretical approach is bottom-up (and points downward), and there are a number of factors that argue persuasively that the bottom-up approach will change the landscape of mass-loss rates considerably in the next few years. These winds of change come from different cardinal points, each of them inherently linked to the 3D reality of a stellar wind. They are steered by recent progress in quantum chemistry and astrophysical observations, and can now build up momentum thanks to the latest developments in supercomputing capabilities.

I do not want to leave this section with the reader feeling that these empirical laws are deceptive or useless. On the contrary! If systematic biases in the retrieval approach can be avoided, the observations tell us the real rates of mass loss. Only after detailed theoretical descriptions are found that reproduce the retrieved rates and relations may the models be used to extrapolate to populations not presently available for study, such as low-metallicity populations in the early Universe. Only then will we have greater faith in our predictions of the maximum luminosity achieved by AGB stars; the mass spectrum of PNe and white dwarfs; the frequency of Type I and Type II SNe,[4] and possibly the masses of their progenitors; and the fate of stellar and planetary companions residing close to the mass-losing red giant primary star. But even if theoretical and empirical mass-loss rate relations agree, we must be extremely vigilant against any confirmation bias in our theoretical efforts.

2.3. Informative Measures Challenging the One-Dimensional World

Our earlier discussion has identified the explicit dependence of the mass-loss rate on fundamental parameters as the nut that needs to be cracked. From the discussion of **Figure 5**, it is clear that

---

[4]A supernova is classified as Type II if the spectrum displays the hydrogen Balmer lines; otherwise it is Type I. When a white dwarf is triggered into a runaway nuclear fusion, caused by the accretion of matter from a binary companion or a stellar merger, it is Type Ia. Type Ib/c and Type II supernovae are caused by the gravitational collapse of the core of a massive star, resulting in a black hole or neutron star.

the theoretical and empirical mass-loss rate prescriptions appear to be similar, but they are in fact intrinsically different. There are challenges ahead of us for there to be a simple gateway between both types of relations, but recent progress in observations and quantum chemistry leads us to believe that the gap between them is not cavernous, and a bridge is gradually but assuredly coming into view. The central pillar of that bridge is the incorporation of a 3D view in all our measures of mass loss, in either the forward or retrieval approaches. As a first step, we need to question whether the retrieved mass-loss rates and relations are reliable. Here, recent progress in observational techniques indicates that there is an elephant in the room—well, actually two elephants, a smaller and a bigger one, which are caught in the act owing to the incredible capacities of novel high spatial resolution observing capabilities. On one hand, there are flow instabilities induced by convection that result in the formation of granulation cells on the surface of the giant stars, and of small-scale density structures in the stellar wind, with sizes of between ∼1 and 50 AU (see **Figure 7**). On the other hand—and encompassing much larger geometrical scales—there is mounting (indirect) evidence that most evolved cool giant stars with measurable mass-loss rates are surrounded by at least one stellar or planetary companion. The companion will perturb the structure of the stellar wind (see **Figure 7**), and will under some circumstances induce an increase in mass-loss rate. As I discuss in Section 4.3, neglecting the 3D structural complexities in retrieval approaches can lead to mass-loss rates that are incorrect by an order of magnitude, which—as we have seen in **Figure 6**—has a huge impact on the outcome of stellar evolution models.

This discussion on the emergence of 3D clumps and the impact of a (hidden) companion provides insight into the deterministic perspective of cool aging stars and their contribution to the chemical enrichment of the Universe. However, there is an additional approach to the how question that could potentially provide useful information for the *why* question as well. By probing what we believe are the early beginnings of a stellar wind, we might be able to grasp the essence of mass loss. To do that, we have to strip the outer layers of complexity, the large 3D structures with scales greater than 1 AU, to uncover what lies beneath. We need to reverse the time axis and dive deeply into the smallest 3D scales that matter. Doing so, we reach the nanometer-sized domain, where dust nucleation is happening (see **Figure 7**). Arriving there, we will discover that, here as well, the bottom-up approach has recently been very instructive in providing new insights into the intricacies of this phase transition, but it requires us to embrace the complexities of the 3D structures of molecules, large gas-phase clusters, and dust grains. Once we arrive at that scale, we may begin to understand *why* cool aging stars contribute to the galactic chemical enrichment and what the driving forces for the complex physicochemical processes governing the Universe are. However, it also will become clear that untangling the tangled web of Schrödinger's equations—describing the transition from molecules to dust—still lies in the distant future.

3. THE EMERGENCE OF THREE-DIMENSIONAL CLUMPS

The first unambiguous observation of structure on the stellar surface of a star other than the Sun was reported in 1990, when Buscher et al. (1990) presented the detection of a bright surface feature on the surface of the RSG Betelgeuse. Betelgeuse has one of the largest apparent angular sizes in the night sky (with a measured angular diameter of ∼44.2 mas in the IR; Dyck et al. 1992), and is an ideal candidate for spatially resolving its surface, not only in the optical but also in the UV and submillimeter wavelength domains (Gilliland & Dupree 1996, O'Gorman et al. 2017). Gilliland & Dupree (1996) interpreted the observed feature as resulting from magnetic activity, atmospheric convection, or global pulsations and shock structures that heat the chromosphere. Recently, another profound realization in observational astronomy occurred through the first image of large granulation cells on the surface of a (much smaller) AGB star, π^1 Gru; our Sun might show some
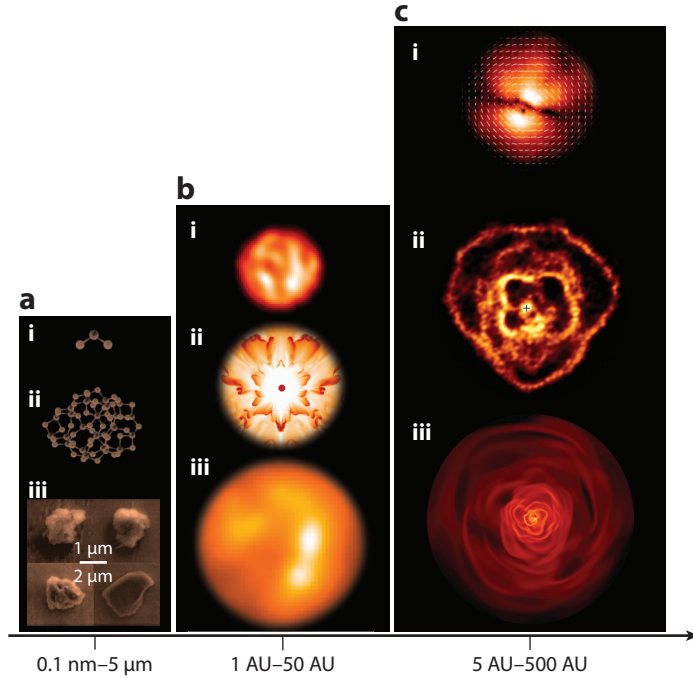
Figure 7

3D structures of relevance for stellar wind research. Compilation based on observations, theoretical calculations, modeling, and laboratory experiments. (*a*) The 3D life of molecules and dust grains: (*i*) TiO_2 proposed as candidate for the first dust condensate in O-rich winds (Jeong et al. 2003, Lamiel-Garcia et al. 2017); (*ii*) global minima candidate for $(TiO_2)_n$ with $n = 24$ obtained within a bottom-up approach by using a global optimization algorithm searching the complex multidimensional potential energy surface (Lamiel-Garcia et al. 2017); (*iii*) presolar corundum grain with AGB origin; image obtained using a scanning electron microscope by Choi et al. (1998). (*b*) The emergence of 3D clumps: (*i*) Due to convection in the stellar atmosphere large granulation cells form on the surface of the O-rich AGB star π^1 Gru and are now seen thanks to the PIONIER instrument mounted at the VLTI (Very Large Telescope Interferometer; Paladini et al. 2018); (*ii*) flow instabilities arising in a 2D model for a dust-driven wind of a carbon star (Woitke 2006a); the red dot represents the AGB star; (*iii*) 2.166-μm image of the carbon star CW Leo obtained with NACO [Nasmyth Adaptive Optics System (NAOS) – Near-Infrared Imager and Spectrograph (CONICA)], mounted at the VLT (Very Large Telescope), showing the presence of small-scale structures (clumps) embedded in the stellar wind (Menut et al. 2007). (*c*) The 3D lasting impact of a companion: (*i*) Detection of an equatorial dust lane in the wind of the carbon star CW Leo using scattered light data obtained by ExPo (Extreme Polarimeter) mounted on the William Herschel Telescope (Jeffers et al. 2014); (*ii*) a rose-like spiral structure detected in the stellar wind of the O-rich AGB star R Hya using ALMA (Atacama Large Millimeter/submillimeter Array; Decin et al. 2020); (*iii*) 3D hydrodynamical simulation for a binary system containing a mass-losing AGB star (El Mellah et al. 2020). Abbreviation: AGB, asymptotic giant branch.

resemblance to π^1 Gru once it becomes a red giant star in about 7.7 billion years. Although the surface of the Sun is covered with about two million convective cells whose typical size is around 2,000 km across, π^1 Gru was shown to have only a few granules with a characteristic horizontal size of about 1.2×10^8 km, or ~27% of the stellar diameter (Paladini et al. 2018). These observations are consistent with the historical prediction by Schwarzschild (1975) that the surface of cool giants might be covered by a relatively small number of giant convection shells. Schwarzschild came to his hypothetical conclusion on the basis of the working hypothesis that the pressure or

density scale heights determine the size of the convective elements. Furthermore, he addressed the question of whether mass ejection could be triggered by photospheric convection. He argued in favor of that suggestion on the basis of observations that provided substantial evidence for nonspherical circumstellar dust clouds in the neighborhood of red giant and supergiant stars, in which the polarized light signal shows variability on the same timescale (of ∼200 days) as the irregular brightness variations caused by the giant convective cells. The cooler regions of the large-scale surface convective elements might enhance the production of dust grains, resulting in an uneven distribution of dust and, hence, of the polarization signal. With this section revolving around the deterministic question and hence aspects of mass loss, we seek to answer whether, in principle, Schwarzschild's argument is settled, and if and how these nonspherical circumstellar dust clouds can be used to trace the mass-loss mechanism.

3.1. Weather Map from Cool Aging Stars: Dry with Variable Cloud Cover

The conjecture by Schwarzschild that there is a potential causal link between the dynamical, inhomogeneous stellar atmosphere driven by convective flows and the formation of clumpy clouds in the CSE can be checked against observational evidence. In the early 1970s, there was only indirect evidence of nonspherical dust clouds in the close vicinity of cool aging stars (Shawl 1972, Schwarzschild 1975), but the new revolution in observational techniques allowed for high-spatial resolution (reconstructed) images and provided direct observational evidence that the CSEs harbor small and large-scale inhomogeneities (for a discussion of large correlated density structures, see Section 4). The CSE of the carbon-rich AGB star CW Leo (at a distance of ∼150 pc) has long been known to be quite complex and continually evolving (see **Figure 7**). As the IR-brightest AGB star experiencing high mass loss, it has been exhaustively studied by many observational techniques. Fine structure on subarcsec scale was detected within ∼30 stellar radii from the central star (Haniff & Buscher 1998, Weigelt et al. 1998). The fragmentation of the shell in distinct clumps was suggested to be caused by inhomogeneous mass loss potentially induced by large-scale surface convection cells. However, the stellar surface and inner CSE of this star are obscured by the optically thick envelope of carbon dust, hindering the identification of the observed clumpy features with processes occurring at the stellar surface, in the shock-dominated inner CSE and in the dust-formation region. Even for carbon stars with a more modest mass loss, IR images can be difficult to interpret, as was shown recently by the example of R Scl (Wittkowski et al. 2017).

The envelopes of O-rich giants tend to be more transparent in the visual and IR wavelength regimes than C-rich giants (see also Section 5), thereby providing better access to the surface and innermost CSE layers and, hence, allowing for a more detailed evaluation of Schwarzschild's conjecture. Observations of scattered light of nearby O-rich AGB and RSG stars establish there are dust clouds as close as ∼0.5 $R_\star$ to the star, whose size is ≲20 $R_\star$ and which change in morphology on timescales of weeks to months (Khouri et al. 2016, Ohnaka et al. 2017a, Adam & Ohnaka 2019, Kamiński 2019, Cannon et al. 2021). The dynamical timescale implied by changes in the circumstellar morphology is in good agreement with the characteristic timescales for convection, and the observed spatial scales (both the size of the clouds and the distance from the stellar surface) compare well with recent 3D RHD models simulating the outer convective envelope and dust-forming region (Höfner & Freytag 2019; see also Section 3.2 for some side notes on this claim). Thanks to these results, we have increased confidence that Schwarzschild's conjecture actually might reflect reality. However, the recent two-dimensional mapping of the velocity field over the surface and inner CSE of the nearby RSG Antares throws a spanner in the works, because the maps reveal vigorous upwelling and downdrafting motions of several huge clumps of gas with velocities ranging from about −20 to +20 km s^{-1} in the inner CSE up to ∼1.7 $R_\star$

(Ohnaka et al. 2017b). Convection alone cannot explain the observed turbulent motions and atmospheric extension, suggesting that a process that has not yet been identified is operating in the extended atmosphere (Arroyo-Torres et al. 2015, Ohnaka et al. 2017b). Admittedly, this result does not rule out Schwarzschild's conjecture, but it reveals that the apparent analogy and the correlation between the surface granulation pattern and the gas and clumps in the extended atmosphere and inner CSE do not in themselves signify a causal relation and conceivably other processes might be important.

3.2. How to Model a Turbulent Life

Whether we consider either a small Sun or a giant star, modeling the turbulent dynamical process of convection and its interaction with other physical, chemical, and radiative processes is a major challenge. This is due to not only the complexity of the problem but also the huge CPU demand dictated by the numerical resolution required for a proper sampling of the time-dependent small- and large-scale fluctuations in density, temperature, velocity, and brightness. Detailed RHD simulations can help us understand qualitatively these processes and model quantitatively the dynamical layers in and around these stars (Freytag et al. 2019). Modeling convection and surface granulation in Sun-like stars is only possible using local 3D RHD simulations owing to the huge disparity in spatial scales and timescales: For a global simulation of a Sun-like star, one would need a spatial resolution of at least a fraction of the photospheric pressure scale height of ∼150 km to cover the Sun (diameter of about 1,400,000 km), and a time resolution of about a second for at least several rotation periods of about a month or, even better, several magnetic cycles, each spanning 22 years (Freytag et al. 2019). In contrast, global 3D RHD models covering the entire convective surface of cool giants are within the realm of possibility, because of Schwarzschild's prediction that only a few giant convection cells cover their surfaces. The first global 3D RHD simulations for a RSG were presented in 2002 (Freytag et al. 2002); the domain of the smaller AGB stars was reached in 2017 (Freytag et al. 2017). These models encompass part of the atmosphere with the outer boundary situated at ∼2 $R_\star$. The model dynamics are governed by the interaction of long-lasting giant convection cells, short-lived surface granules, and radial fundamental-mode pulsations (see also Section 2.2.3). The models did not yet include dust formation and therefore no wind driving. Recently, a global model for an oxygen-rich AGB star was presented that incorporates both the outer convective atmosphere and the dust-forming region up to ∼2.8 $R_\star$ (Höfner & Freytag 2019). The current models do not yet describe wind acceleration, and the kinetic treatment of grain growth does not account for nucleation but assumes the presence of seed particles. I expand on the challenge of dust nucleation shortly (Section 5), but for the time being it is sufficient to realize that we are still speculating as to the specific steps of seed formation. In the models, grain growth is hypothesized to take place under the most optimum circumstances (sticking coefficient assumed to be one; see also Section 5.3.1).

Although the 3D RHD models including dust growth still have some limitations, already they offer great insight into the essence of mass loss at least for stars on the upper AGB and in the RSG phase, where stars have the lowest surface gravities and, hence, the largest pressure scale heights and largest granules relative to the stellar radius. The large-scale convective flows and pulsations generate atmospheric shock waves: the shorter-wavelength disturbances cause a complex small-scale network of shocks in the innermost layers, whereas the fundamental-mode pulsation causes a more or less spherical shock front that is able to travel further away from the stellar surface. In the dense wake of the shock, gas is temporarily lifted to distances at which dust formation may occur (Freytag et al. 2017). Remarkably and importantly, the temperature shows a rather smooth, almost spherical pattern, in contrast to the gas densities, which are strongly affected by the local

3D dynamics and show a pronounced 3D clumpy morphology (Höfner & Freytag 2019). Only when the temperature falls below a critical value does the gas become supersaturated. Under supersaturation, the molecules are more prone to leave the gas than to rejoin it, so they become deposited on the surface of the solid particles and grain growth is triggered. Because the temperature acts as a threshold for the onset of grain growth, whereas the gas densities determine the grain growth efficiency, the models show an almost ring-like dust number density distribution conditioned by the local temperature. For a 2D slice through the center of the grid, the dust layers appear narrow in the radial direction due to the rapidly decreasing densities with increasing distance. Even then, smaller patches of dust clouds appear where both the density and radius of the grains vary in response to the local gas density and velocity. This behavior is characteristic not only of O-rich environments; 2D carbon-rich wind models also show a similar pattern (Woitke 2006a; see **Figure 7**).

Supersaturation: a gas–solid or gas–liquid chemical system that is in a nonequilibrium state such that there are too many gaseous molecules for the present temperature–pressure conditions

Given the fact that the models of Freytag et al. (2002, 2017) and Höfner & Freytag (2019) do not include the radiation pressure on dust grains, they do not directly address the speculation by Schwarzschild that mass ejection could be triggered by photospheric convection. However, given the results just described, I argue here that clumps generated by convective motions are not the cause or the essence of mass loss; rather they are the consequence of the local 3D atmospheric conditions. This argument is based on (*a*) the isotherms, which are set by nonlocal radiative processes, being nearly perfect spheres and (*b*) the consideration that not only the onset of the dust growth but also, even more elementally, dust nucleation is dictated by the local temperature (see Woitke 2006a, their figure 8; see also Section 5.3.2). Convection-induced 3D cloudy structures are of second order for wind driving in the sense that grain growth can be locally of higher or lower efficiency due to a change in density, but as long as the gas is not supersaturated no force can be generated that overcomes the stellar gravitational attraction. This argument rests on the common idea of a dust-driven outflow, which is more appropriate for AGB than RSG winds. For RSG stars with their very low surface gravities the situation might be the reverse. A recent study shows that inferred atmospheric turbulent velocities yield turbulent pressure high enough to initiate mass loss even in the absence of circumstellar dust (Kee et al. 2021). In this regard, and for these fluffy RSG stars, Schwarzschild's conjecture still holds—but is not yet proven—and photospheric convection seems to be a viable mechanism to trigger mass ejection.

3.3. Impact on Derived Properties

Clumps show up not only in the inner CSE; they are also present at much larger distances from the star—i.e., up to the bow shock, where the stellar wind collides with the ISM (Cox et al. 2012; Decin et al. 2016, 2018b; Kamiński 2019; Montargès et al. 2019). At present, it is still not understood which mechanism prevents clumps, which are formed in the inner CSE, from dissipating during their travel through the huge CSE. Potentially, clumps can cool very efficiently, inducing a reduction of the internal pressure. But even without understanding the process, we are in principle able to quantify the impact of 3D clumps on mass-loss rate retrieval efforts by carefully measuring the amount of mass in the clumps and the surrounding smooth envelope. However, the need for highly performant 3D radiative transfer analysis often steers scientists toward simplistic analytic estimates. A small mistake in the optical depth, however, might have a substantial impact on the mass estimates because the optical depth enters in the exponent of the intensity estimate [$I_\nu \propto S_\nu \exp(-\tau_\nu)$]. This leaves us with only a few examples, all RSG stars, to guide us in this exercise. These analyses indicate that clumps contribute from a few up to $\sim$25% of the total mass loss (Ohnaka 2014, Montargès et al. 2019, Cannon et al. 2021); the only potential exception is the extreme RSG VY CMa for which the derived dust mass in the clumps (of 0.47 $M_\odot$)

seems unrealistically high to be compatible with a current stellar mass of 17 $M_\odot$ (Kamiński 2019). With the exception of VY CMa, this suggests that the mass loss in ejected clumps contributes nonnegligibly to the total mass loss, but also that the clumps do not represent the main mass-loss mechanism. This conclusion reinforces the final statement in the preceding section: Convective-induced turbulent pressure might invoke mass ejection for RSG stars, but in all its generalities that mechanism only depends on the turbulent velocities and has no significant explicit dependence on any 3D clump characteristic.

Given this (tentative) outcome and the substantial struggle for deriving reliable mass-loss rate relations (as described in Section 2.2.4), it seems fair to conclude that the story of 3D clumps only bears limited relevance for both the deterministic and conceptual questions. However, this is too short-sighted for several reasons. First, forward theoretical models predict a considerably different molecular abundance pattern whether clumps are included or excluded (Agúndez et al. 2010, Van de Sande et al. 2018b), where notable examples include the formation of water (H_2O) molecules in a carbon-rich wind and hydrogen cyanide (HCN) in O-rich envelopes at sufficiently high abundances to be detected with very sensitive telescopes. These predictions not only are consistent with contemporary observations (e.g., Lombaert et al. 2016, Van de Sande et al. 2018a) but also convey the message that our estimate of the chemical enrichment of the ISM by cool aging stars is at best preliminary.

Second, stars do not stand still. Instead stars travel through the ISM, where a striking testimony is the appearance of bow shocks that are so beautifully imaged with the *Herschel Space Observatory* (Cox et al. 2012). The difference in velocity and density between both media invoke the growth of Rayleigh–Taylor and Kelvin–Helmholtz instabilities, and kinetic temperatures are estimated to reach up to 10,000 K, depending on the shock velocity v_S (van Marle et al. 2011, Decin et al. 2012). This might foster the dramatic idea that the collision with the ISM can destroy any relic of the chemical processes occurring in stellar winds, because molecules can break up (dissociate) and grains can be destroyed. However, this is only true for the most violent collisions and even then the larger grains are shown to survive (van Marle et al. 2011), leaving us with a grain-size distribution modified toward larger grains. For low-velocity collisions ($v_S \leq 5$ km s^{-1}), most of the kinetic energy dissipates via magnetic compression and through the rotational emission of molecules such as CO and H_2O or the fine structure lines of C^+ and O (Godard et al. 2019). As the velocity increases, H_2 becomes the dominant coolant over a wide range of shock velocities and gas densities (Lesaffre et al. 2013, Flower & Pineau des Forêts 2015). The general outcome is a higher fraction of ionized atoms, excited molecules, and sputtered grains. Returning to the persistent clumps and their importance for the deterministic aspect, if material is embedded within higher-density clumps, it will be less affected by the collisions that occur in the bow shock, by the harsh interstellar UV field, and by the possible entwinement of radiative and mechanical energies. In other words, clumps do not only help us diagnose the genuine wind chemistry; they are also a key ingredient for quantifying the galactic chemical evolution and are, as such, of fundamental importance for the deterministic question.

4. THE THREE-DIMENSIONAL LASTING IMPACT OF A PARTNER

While the smaller elephant (a.k.a. the 3D clumps) seems part of the furniture with limited repercussions on mass-loss rate estimates—but with a profound effect on chemical processes—there is still that other, bigger elephant, which came into view owing to the detection of large correlated density structures in stellar winds, and which exposes the scientific quandary that modern astrophysics has been contending with in recent years. It has been more often than not that unexplained phenomena in observational astrophysics were either justified or, conversely, neglected by using

the phrasal idiom "...binarity which is not within the scope of this paper (or conference talk)"; magnetic fields suffer the same fate. Our Sun with its eight planets has no (known) stellar companion. So akin to social psychology, where it is well known that humans tend to hire job candidates on the basis of similarities to themselves (the "similarity attraction bias"), a general thesis that formed the basis for stellar evolution models took shape, namely that solar-like stars live their lives alone (and the planets are inconsequential for the late stages of evolution). In retrospect, that thesis now appears to be problematic, especially if we are pondering the fate of solar-like stars experiencing substantial mass loss on the AGB. I will venture the idea that a planetary or stellar companion impacts the wind morphology of almost all AGB and RSG stars with a detectable mass-loss rate ($\dot{M} \gtrsim 10^{-7}$ M$_\odot$ year^{-1}). Furthermore, in a fraction of stars the companion induces a change in expansion velocity and mass-loss rate. This implies that most empirically derived mass-loss rates are obtained from samples containing a large fraction of stars that experience binary interaction with a (sub-)stellar companion. Therefore, our knowledge of the mass-loss rate is biased by the impact that companions can have on the strength of the mass loss and on the observed diagnostics from which mass-loss rate values are retrieved. It goes without saying that this viewpoint touches directly on the deterministic question, and—unlike the small elephant—this time we will not be bogged down in the minutiae of detail; a partner changes your life once and for all.

4.1. The Key to Finding the Invisible Partner

Binary companions orbiting mass-losing AGB stars somehow managed to escape the scientific picture. Every so often, the presence of a companion was invoked to explain the metamorphosis from an overall spherical AGB wind to the aspherical morphologies seen in their descendants, the post-AGB stars and the PNe. Indeed, already the first photographic atlas of PNe, published in 1918 by Curtis, showed an astonishingly wide range of PN morphologies and led Curtis (1918, p. 67) to question whether "it is possible to postulate any general form or forms, which shall be mechanically plausible, and to which the planetaries, or a considerable proportion of the planetaries, will more or less closely conform." Since then, the quest for the primary mechanical cause shaping PNe has been open. Whereas ~80% of AGB stars have a wind with overall spherical symmetry (Neri et al. 1998), less than 20% of PNe possess a circular symmetry (Parker et al. 2006, Sahai et al. 2011). We point out a few prominent examples imaged by, for example, the *Hubble Space Telescope* (HST): The inner structure of the Eskimo Nebula, a bipolar double-shell PN, shows a complex rose-like structure (O'Dell et al. 2002), whereas the Helix Nebula is a bipolar PN with an eye-like morphology (O'Dell et al. 2004, Su et al. 2007). Biconical shapes are seen in various post-AGB stars and PNe, including the post-AGB star IRAS 17150−3224, which also has a highly equatorially enhanced shell (Ueta et al. 2007), and the Owl Nebula (NGC 3587), a PN that has a barrel-like structure in its inner shell caused by bipolar cavities (Guerrero et al. 2003). The Red Rectangle is an O-rich post-AGB binary system that has a Keplerian (rotating) disk and an outflow, the latter mainly being formed of gas leaving the disk (Bujarrabal et al. 2016); in its outer halo, regularly spaced arcs embedded in a bipolar outflow are detected (Cohen et al. 2004).

For a long time, the development of these nonspherical structures during the post-AGB and PNe phases has been a matter of debate. Several contending theories attempted to explain this morphological metamorphosis, including rapid stellar rotation and strong magnetic fields in single-star models (García-Segura et al. 1999), as well as binary models with a particular focus on short-period binary systems formed after a common-envelope phase (orbital period $P_{\text{orb}} \lesssim 10$ days; Soker 1998, Miszalski et al. 2009). Even for the first two mechanisms, the presence of a binary companion is sometimes called upon to sustain the mechanism (Soker & Harpaz 1992). In principle, the material ejected during the AGB phases does not have enough angular momentum

BINARY INTERACTION

Although this is not the place to present a detailed physico-chemical description of binary interaction, the key point is easy to state: The gravitational potential of the companion alters the equation of motion, and if the companion is UV-active, which is likely if it has lost its envelope, it can impact the chemistry of the surrounding envelope. The concept of Roche-lobe overflow (RLOF) has proven powerful in the description of binary evolution. The critical equipotential surface in the Roche potential, passing through the inner Lagrangian point L_1, defines two Roche lobes surrounding each star. The volume-averaged radius of the Roche lobe can be approximated to an accuracy of better than 1% following Eggleton's formula (1983):

$$\frac{R_{L1}}{a} = \frac{0.49\, q^{2/3}}{0.6\, q^{2/3} + \ln(1 + q^{1/3})},$$

where q is the mass ratio M_1/M_2, and a the orbital separation. Mass-transfer interaction from the primary to the secondary can be classified into four types in increasing order of interaction: Bondi–Hoyle–Lyttleton (BHL) accretion (Hoyle & Lyttleton 1939, Bondi & Hoyle 1944), wind-Roche lobe overflow (WRLOF; Podsiadlowski & Mohamed 2007), RLOF when the Roche lobe surface is connected (Paczyński 1971), and common envelope evolution Ivanova et al. (2013). It is believed that for wide binary systems ($a \geq 2$ AU) the mass transfer does not occur through RLOF but via WRLOF, in which case wind material from the mass-losing AGB star fills the giant's Roche lobe and is transferred to the companion through a compressed channel that generally does not pass through L_1.

to form Keplerian disks, which should only appear around binary stellar systems, as these systems have the necessary angular momentum stored in their orbital movement. Axial structures in the form of collimated fast winds have subsequently been proposed to be associated with such rotating disks, from which material would fall onto the star or a companion during early post-AGB phases, powering very fast and collimated stellar jets (Bujarrabal et al. 2001, Soker 2001, Balick & Frank 2002). Most of these proposed PN shaping processes act on the AGB star itself, and each of them is thought to operate over a short time, during the final few hundred years of either the AGB phase or the early post-AGB phase. The short lifetime of the post-AGB and PN phases, the strong observational bias toward detecting short-period binary post-AGB stars and PNe, and the high mass-loss rates at the end of the AGB phase leading to an obscuration of the inner workings made the identification of the shaping mechanism and its time of occurrence observationally challenging.

Aiming to understand some of the observable characteristics of axisymmetric or bipolar post-AGB stars and PNe, Mastrodemos & Morris (1999) were the first to perform pioneering hydrodynamical simulations of dusty red giant winds in detached binary systems ($P_{orb} \gtrsim 1$ year), in which the effects of the companion are manifested on the wind of the red giant rather than the star itself. (See the sidebar titled Binary Interaction.) In these simulations, the primary star was a mass-losing red giant star and the companion's mass was in the range of 0.25–2 $M_\odot$ with orbital separation of 3–24 $R_\star$. They derived a range of envelope geometries encompassing bipolar, elliptical, and quasi-spherical geometries characterized by a continuously decreasing density contrast between the equatorial plane and the poles. The last category manifested a novel type of hydrodynamic wind solution in the form of a spiral shock caused by the reflex motion of the mass-losing AGB star. Depending on the system's parameters and the inclination angle of the system, the 2D projection of these spirals in the plane of the sky appears as an Archimedes spiral or as a series of rings in the wind. The year 1999 was also when the first-ever multiple, incomplete, concentric shells were detected in the envelope of the carbon star CW Leo ($\dot{M} \sim 1.5 \times 10^{-5}$ $M_\odot$ year^{-1}) using the HST (Mauron & Huggins 1999). Probably unaware of the results by

Mastrodemos & Morris (1999), Mauron & Huggins (1999) attributed the shells to mass-loss modulations with a timescale of ~200–800 years, caused by an undefined episodic process intrinsic to the star. The impact of a binary companion was tentatively suggested but was deemed insufficient to explain the structure of the shells farther out. Searching for the cause of the episodic process, Simis et al. (2001) suggested that an intricate nonlinear interplay among gas-grain drift, grain nucleation, radiation pressure, and envelope hydrodynamics can result in gas and dust density shells that occur at irregular intervals of a few hundred years for a single-star model. However, the predicted shell density variations were much larger than the observed ones (Decin et al. 2011).

It took an additional seven years before the same authors, Mauron & Huggins, reported in 2006 the detection of the first conspicuous Archimedes spiral pattern in the wind of a carbon-rich AGB star (AFGL 3068; $\dot{M} = 4.2 \times 10^{-5}$ M$_\odot$ year^{-1}). This discovery was, and still is, highly significant and led to the unequivocal conclusion that binary interaction shapes the stellar wind during the AGB phase, and as such plays a role in carving out PNe. However, despite presenting this and analogous results (see below) to the scientific community, there still remains a fraction of skeptical astronomers because the companion remains invisible to current instrumentation. As a renowned German astrophysicist told me after my lecture on February 7, 2020, "You know, Leen, it all looks so fantastic, the observations are so fascinating, the current state-of-the-art models seem to do a pretty good job for interpreting the data, but in the end shouldn't we only believe what we actually can see?" I remember that fraction of a second during which the old saying of Edgar Allan Poe (1845, p. 194) jumped into my mind, "Believe nothing you hear, and only one half that you see," but finally found myself arguing that much of astrophysics remains in the realm of conjectures, even Einstein's theory of general relativity (1915) or, to bring it closer to my own field of expertise, even the fact that we believe that AGB stars are the ancestors of PNe. In a few exceptions, such as o Ceti or W Aql, the binary companion is actually seen (Karovska et al. 1993, Ramstedt et al. 2011), but the high luminosity outshines the faint companion for most sources. The *Gaia* parallax's measurements can potentially give us some light at the end of the tunnel if corrections can be made for the turbulent AGB and RSG atmospheres (Kervella et al. 2019).

The opening of ALMA in 2012 heralded a leap forward in the understanding of wind morphologies. Observational evidence was steadily accumulating that AGB and RSG winds exhibit large correlated density structures—including arcs, shells, bipolar structures, tori, rotating disks, and spirals—embedded in a smooth, radially outflowing wind (see **Figure 7**) (Maercker et al. 2012; Ramstedt et al. 2014, 2018; Decin et al. 2015, 2019; Kim et al. 2015; Kervella et al. 2016; Wong et al. 2016; Bujarrabal et al. 2018; Guélin et al. 2018; Homan et al. 2018a,b; Randall et al. 2020). At the same time, we saw a revival of hydrodynamical simulations for binary systems in which the primary is a mass-losing AGB star. Depending on the parameters of the system—such as binary separation, mass ratio, eccentricity, rotation and pulsations of the AGB star, mass-loss rate, wind velocity, etc.—a wide variety of morphologies is predicted, including the following: (*a*) a spiral structure caused by the orbital motion of the mass-losing AGB star around the common center of mass, or by the accretion wake of the companion owing to a BHL flow (see **Figure 8**) that can be bifurcated for a noncircular orbit; (*b*) a circumbinary disk; (*c*) an accretion disk around the secondary; (*d*) a bipolar outflow that can display ripple-like structures if the AGB pulsations are included; (*e*) an equatorial density enhancement (EDE), with a regular (Keplerian) or complex velocity vector field; and (*f*) even spider or rose-like structures (see **Figure 7**; Kim & Taam 2012, Chen et al. 2017, Liu et al. 2017, Saladino et al. 2018, Saladino & Pols 2019, Kim et al. 2019, Chen et al. 2020, El Mellah et al. 2020). In general, smaller values of the orbital separation or wind velocity and larger companion masses induce stronger interaction. These outcomes can be formally expressed in a way similar to Equation 13 or Equation 16, although it is obviously seen that the number of independent parameters is far larger. Therefore, the amount of studies in which the

model sensitivities can be tested for a large grid of parameters is still very restricted by the huge demand on CPU time and memory required.

The resemblance between the observed and theoretical morphologies supports the claim that binary interaction is a key architect of AGB and RSG wind shaping. However, it should also be acknowledged that the observations are often more complex than any model prediction, owing to simplification in the models and to the fact that other mechanisms, such as magnetic fields, might contribute to an initial wind anisotropy. Generally, deducing the model functions from the behavior of a complex system is an inverse problem that is difficult to solve, but I contend that this approach will see significant growth in the coming decade thanks to increasing CPU power and, in particular, the use of artificial intelligence; see for example the paper by de Mijolla et al. (2019).
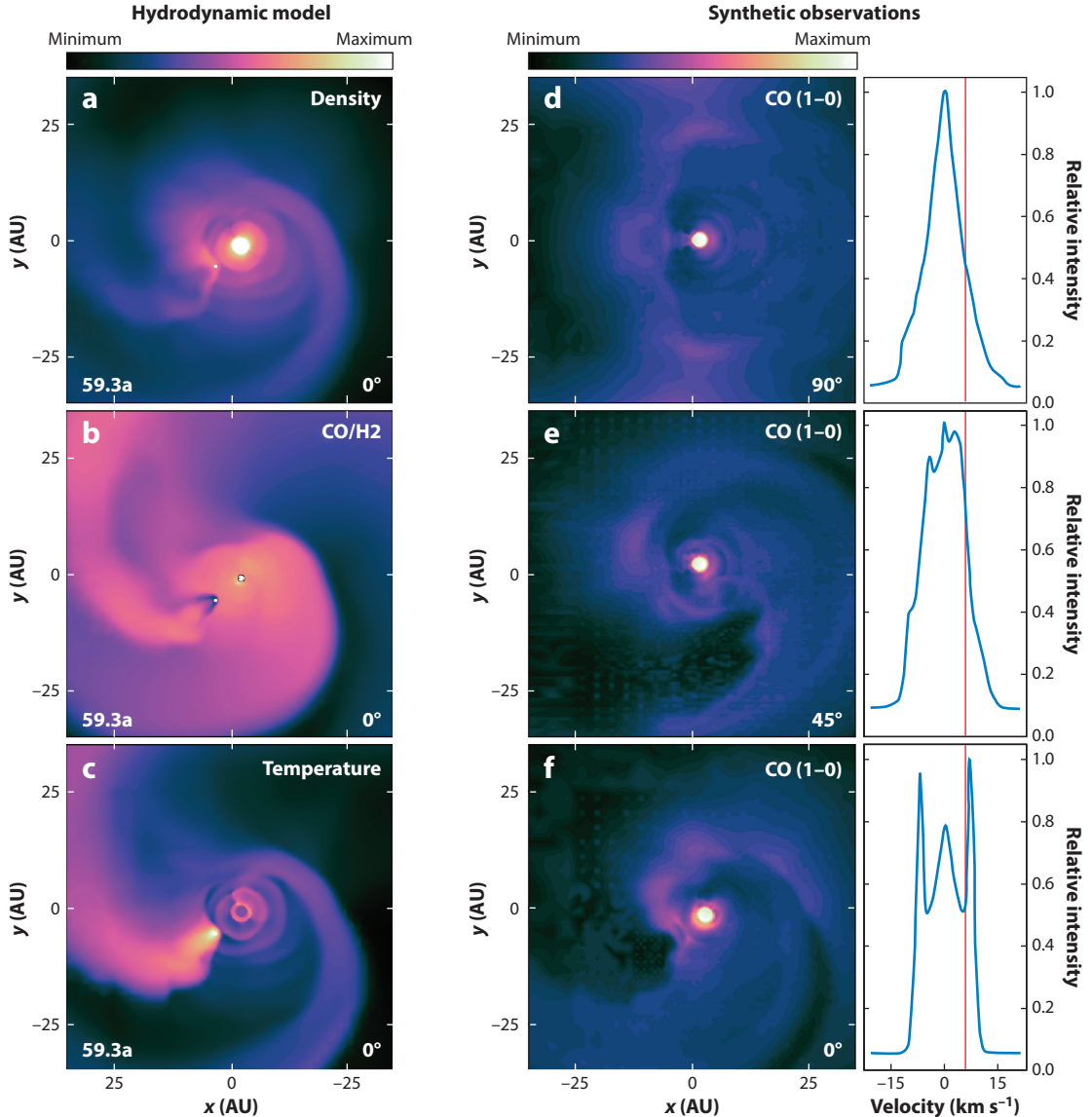
(*Caption appears on following page*)

Figure 8 (*Figure appears on preceding page*)

3D hydrochemical simulation for a binary system containing a mass-losing AGB star. The left panels are from **Supplemental Video 1** showing (*a*) the total density; (*b*) CO/H$_2$ number density; and (*c*) temperature for a binary system model in which the AGB star has a mass of 1 M$_\odot$, effective temperature of 2,900 K, a radius of 0.9 AU, and a pulsation period of 1 year. The companion has a mass of 0.5 M$_\odot$ and resides at a circular orbit with separation of 10 AU. The simulation time runs for 59.3 years. Owing to dust formation occurring in the region where the temperature is lower than 1,500 K, a wind is initiated with mass-loss rate of 4.7×10^{-6} M$_\odot$ year^{-1}. The formation of two types of spiral structures can readily be seen, one structure being caused by the gravity wake near the companion, the other one caused by the reflex motion of the AGB star. Both spiral structures merge at larger distances from the AGB star. The small ripples in the close vicinity of the AGB star are relics of the pulsation pattern. The same setup for the AGB star not having a companion yields a mass-loss rate of 7.6×10^{-7} M$_\odot$ year^{-1} (J. Bolte, L. Decin, W. Homan, F. De Ceuster, J. Yates, et al., in preparation). For a simulation time of 59.3 years, the hydrodynamical quantities are then displayed for viewing angles of the system ranging between 0 deg (edge-on view) and 90 deg (face-on view). The right panels show the corresponding CO $v = 0$, $J = 1$–0 emission map and line profile at $t = 59.3$ years for three different viewing angles [at 90 deg (*d*), at 45 deg (*e*), and at 0 deg (*f*)] in the observer's frame calculated using the MAGRITTE 3D radiative transfer solver (De Ceuster et al. 2020a, 2020b). The video slices through the velocity channel map between -20 and $+20$ km s^{-1}. Figure courtesy of F. De Ceuster and J. Bolte. Abbreviation: AGB, asymptotic giant branch.

A systematic approach will not only elucidate the intricacies of binary interactions based on theoretical predictions; the same truism holds for observations. In 2018, the ALMA ATOMIUM[5] Large Programme was granted substantial time on the telescope and a well-selected sample of oxygen-rich AGB and RSG stars was observed in a systematic and unbiased way with the specific aim of understanding the thermodynamical, chemical, and morphological properties of their stellar winds (Decin et al. 2020; also C.A. Gottlieb, L. Decin, A.M.S. Richards, S.H.J. Wallström, T. Danilovich, et al., submitted). The ATOMIUM data revealed that all of the AGB winds observed exhibit distinct aspherical geometries (see **Figure 9**), which have morphological counterparts in the PNe. This led to the inference that the same physics is key in shaping both AGB winds and PNe. The ATOMIUM data catch the wind-shaping mechanism in the act and constrain the moment in time when AGB morphologies are being transformed into nonspherical geometries. A strong statistical correlation emerges between the AGB mass-loss rate and the prevailing geometry (Decin et al. 2020): A dynamically complex EDE is often observed for oxygen-rich AGB stars with low mass-loss rates ($\dot{M} \lesssim 10^{-7}$ M$_\odot$ year^{-1}; defined there as "Class 1"), and a bipolar structure tends to be dominant for stars with medium mass-loss rates ("Class 2"; 10^{-7} M$_\odot$ year^{-1} $\lesssim \dot{M} \lesssim 10^{-6}$ M$_\odot$ year^{-1}), whereas the wind of high mass-loss rate stars preferentially exhibits a spiral-like structure ("Class 3"; $\dot{M} \gtrsim 10^{-6}$ M$_\odot$ year^{-1}). This correlation and the observed characteristics are readily explained by binary interaction. The results allowed Decin et al. (2020) to propose an evolutionary scenario for AGB wind morphologies in which early-type AGB stars will often be characterized by an EDE, with complex flow patterns (Class 1), and the wind of late-type high mass-loss rate AGB stars will mainly be shaped by spiral structures (Class 3). The proposed evolutionary scheme for AGB wind morphologies can explain various AGB, post-AGB, and PN phenomena, including for instance why post-AGB star binaries can have nonzero eccentricities (Decin et al. 2020). The binary scenario gets support from an analysis of the kinematic wind properties (C.A. Gottlieb, L. Decin, A.M.S. Richards, S.H.J. Wallström, T. Danilovich, et al., submitted). Furthermore, it was shown that early-type AGB stars with a low mass-loss rate are prime candidates for detecting planets. This prediction aligns with the detection that Jupiter-sized companions reside in the near vicinity of the low mass-loss rate AGB stars L$_2$ Pup and R Dor (Kervella et al. 2016, Homan et al. 2018a).

In any case, regardless of the classification proposed by Decin et al. (2020), it should be emphasized that the same set of observations may on occasion be interpreted in different ways and may lead to the recognition of different categories. An immediate example might be that instead
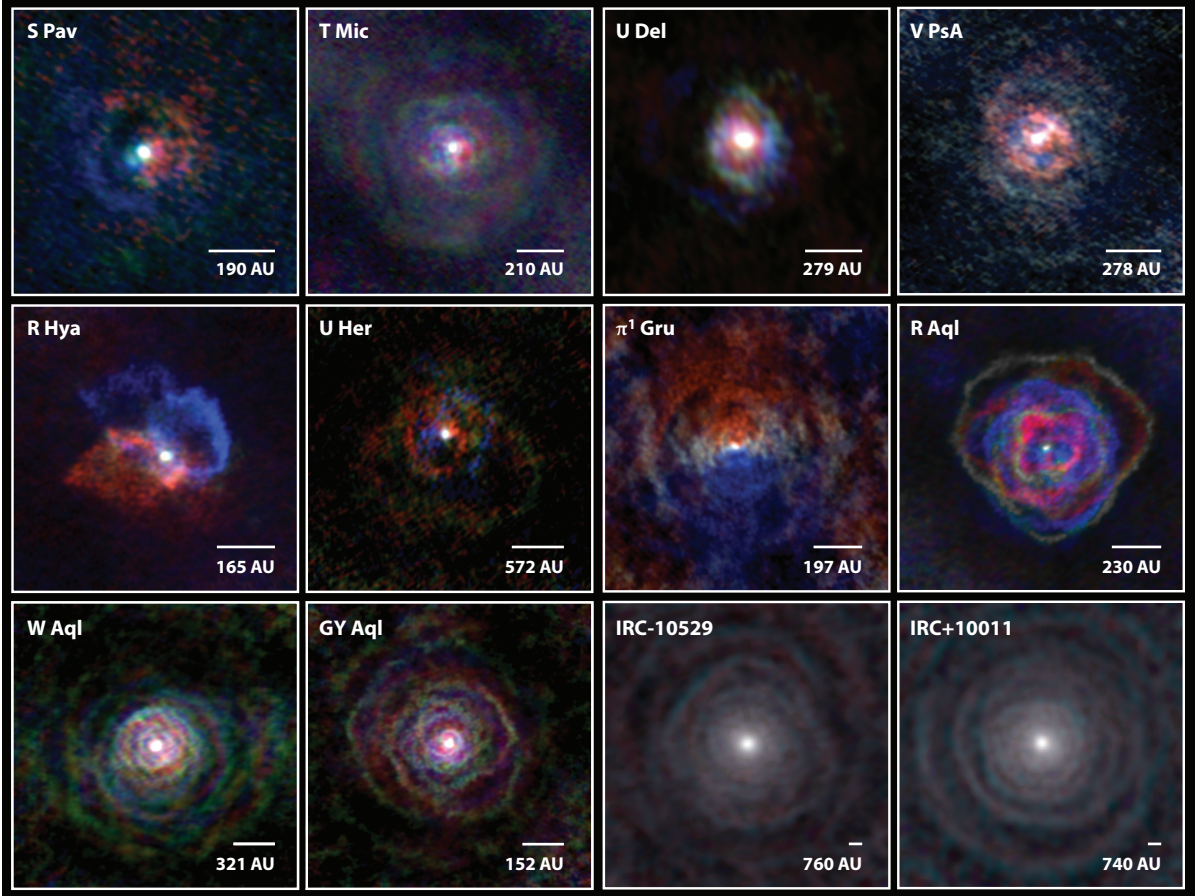
Supplemental Material >

Figure 9

Gallery of AGB winds. Emission maps of 12 AGB stars are shown, derived from the ATOMIUM ^{12}CO $v = 0$, $J = 2$–1 data. For each star, emission that is redshifted with respect to the local standard of rest velocity is shown in red, blueshifted emission is in blue, and rest velocity is in white. The scale bars have an angular extent of 1 arcsec. Sources are ordered by increasing mass-loss rate, from left to right, and from top to bottom. Figure based on Decin et al. (2020), their figure 1. Abbreviation: AGB, asymptotic giant branch.

of the mass-loss rate, the wind acceleration is of greater importance for dictating the morphological outcome (see the discussion in Decin et al. 2020, their section S3.3). When a system can be categorized in more than one way, the question as to which category is better may depend on the particular phenomenon under study. The mapping is probably not simple, and the sample size needs to be significantly expanded before we can investigate the statistical aspects in detail.

4.2. Statistics to Probe the Invisible

The following logical proposition ($\models \mathcal{S} : A \lor \neg A$) is a clear tautology of propositional logic as introduced by the great twentieth-century philosopher Ludwig Wittgenstein (1921) in his famous *Tractatus*. This logical tautology can be paraphrased by saying "a star has either at least one companion, or a star lives its life alone." I am of the view that this tautology might vanish in the foreseeable future with only the first part remaining—not only for massive stars, for which it has been established that binary interaction dominates their evolution (Sana et al. 2012), but also for

Table 1 Summary of main-sequence (sub-)stellar multiplicity fraction[a]

Main-sequence initial mass	Spectral type	Stellar companions	Brown dwarfs	Planets $M > 5\,M_{Jup}$	
				$a = 2$–10 AU	$a = 10$–100 AU
$0.8 < M_{ini} < 1.5\,M_\odot$	FGK	$\sim$30–37%	$\sim$0.8%	$\sim$7%	$\sim$9%
$1.5 < M_{ini} < 8\,M_\odot$	AB	$\sim$52–60%	$\sim$0.8%	$\sim$7%	$\sim$40%

[a]Columns 1 and 2 give the main-sequence initial mass and related spectral type on the main sequence. Columns 3–6 list the (sub)-stellar multiplicity fraction for companions with $\log P_{orb}$(days) $<$ 6.5 and $\log P_{orb}$(days) $>$ 2.7 (or 3) in the case of planets (respectively, stars).

the low- and intermediate-mass stars, which are the focus of this review. It is quite obvious that this statement is inspired by one of the most significant developments in modern astronomy, which is that we seem to find planets around stars almost everywhere we look. To assess this hypothesis, we consider another discipline in mathematics: statistics.

We therefore summarize the current state of knowledge concerning the occurrence rate of stellar and planetary companions around low- and intermediate-mass stars. To do so, I borrow heavily from Decin et al. (2020, their supplementary material, section S5) and references therein. For convenience, I here reproduce **Table 1**, which focuses on stars with initial mass, M_{ini}, in the range of 0.8–8 $M_\odot$. It is well established that the binary fraction increases for higher initial masses, in this case for the more massive stars with $M_{ini} \gtrsim 8\,M_\odot$ that will evolve to the RSG stage, and that some fractions listed in **Table 1** might be lower limits owing to limitations in detection techniques.

Table 1 is constructed on the arguments that we are looking at those binary systems for which the orbital separation (and hence orbital period P_{orb}) and the companion mass are such that hydro-dynamical simulations indicate a perturbation of the smooth envelope structure. This leads to the conservative estimate of $\log P_{orb}$(days) $<$ 6.5 and $\log P_{orb}$(days) $>$ 2.7 (or 3) in the case of planets (or, respectively, stars). Using these boundaries, we assess the main-sequence stellar and substellar multiplicity factor (see **Table 1**; Moe & Di Stefano 2017, Fulton & Petigura 2018, Fulton 2019, Nielsen et al. 2019). In a final step, one should account for the evolution of the (sub-)stellar binary fraction from the main sequence to the AGB (and RSG) phase. A rough estimate is that the binary fraction will decrease by $\sim$10–20% as stars evolve toward and on the AGB and/or RSG phase (Decin et al. 2020).

A last realization is adopted from population statistics. Based on stellar evolution models, it can be argued that the majority of AGB (and RSG) stars with a mass-loss rate above $10^{-7}\,M_\odot$ year^{-1} are of mass above 1.5 $M_\odot$ (Decin et al. 2020). Stars of lower mass will only have a very short period in their AGB phase during which the mass-loss rate is greater than $10^{-7}\,M_\odot$ year^{-1} before they transit into the PN phase, limiting their detection probability. Combining this outcome with **Table 1** leads to the specific conjecture that most AGB stars with mass-loss rate above $10^{-7}\,M_\odot$ year^{-1} have masses above $\sim$1.5 $M_\odot$ and hence have, on average, $\gtrsim$1 companion(s) with masses above $\sim$5 M_{Jup}. Hence, (sub-)stellar binary interaction is the prime wind-shaping agent of the majority of cool aging stars for which the mass-loss rate exceeds the nuclear burning rate ($\dot{M} \gtrsim 10^{-7}\,M_\odot$ year^{-1}), in which case mass loss rules stellar evolution (Decin et al. 2020).

In conclusion, it took us some time to realize that roses flourish during the end stages of stellar evolution (see **Figure 7**), but to quote one of the best-selling and most translated books ever published, "C'est le temps que tu as perdu pour ta rose, qui fait ta rose si importante" (i.e., "It's the time you spent on your rose that makes your rose so important"; de Saint-Exupéry 1943). The

question then is how that rose impacts our deterministic insight in the mass-loss rate of AGB and RSG stars.

4.3. How Can a Companion Change a Stellar Life?

Indeed, the stellar and planetary companions not only serve to beautify the stellar winds during the end stages a star's life but they can also have a direct impact on the star's evolution. For close binary systems, a stellar companion or a massive planet can enhance the mass-loss rate by depositing angular momentum into the envelope and reducing the effective gravity of the mass-losing star. Stars that are born single or binary stars isolated from angular momentum deposition hence might suffer from a lower mass-loss rate than stars prone to angular momentum deposition (Sabach & Soker 2018); for the example shown in **Figure 8**, this effect is a factor of about six. This conclusion has a serious repercussion on any empirically retrieved mass-loss rate relation discussed in Section 2.2.4. Building on the discussion in Section 4.2, we conjecture that most empirically retrieved mass-loss rates yield mass-loss rate measures that are too high for application in single-star evolution models, because samples of stars will be flawed by a large fraction of stars that experience binary interaction (C.A. Gottlieb, L. Decin, A.M.S. Richards, et al., submitted). This brings us back to one of the pitfalls of retrieval approaches outlined in Section 2.2 and the caution expressed there about unrecognized bias effects in sample selections and the elemental difference between correlation and causal effects.

There is a second no less fundamental problem with empirically retrieved mass-loss rates in the case of unrecognized binary interaction. For a mass-losing AGB and/or RSG star in a binary system, the material will have a directional preference toward the orbital plane, and an EDE will form. The density contrast between the equator and the pole increases for smaller orbital distance, lower wind velocity, and higher companion masses (El Mellah et al. 2020), with density contrasts up to an order of magnitude. However, dust mass-loss rates—which in a next step are converted to gas mass-loss rates—are most often derived from the analysis of near- to mid-IR SEDs that mainly trace warm dust residing close to the (primary) star, hence in the EDE (Decin et al. 2019). Therefore, the analysis of dust spectral features with a simplified 1D approach reflects the higher density in the EDE created by the binary interaction but not the actual mass-loss rate, which will be lower by up to an order of magnitude (Wiegert et al. 2020). This deduction amplifies the resolution of the previous paragraph and leads to the inference that scientists modeling single-star evolution by applying empirically retrieved mass-loss rate formulae should be very cautious because the rates might be seriously overestimated. It is readily seen that this conclusion directly impacts any estimate of the chemical enrichment of the ISM by cool aging stars. In what follows, I make some suggestions and predictions that flow directly from the above conclusions.

The only prescriptions currently devoid of a binary-induced bias are the theoretical and—to a large extent—the semiempirical mass-loss rate formulae (see **Figure 5**). However, these mass-loss rate prescriptions for AGB stars are only meant to describe the properties of Mira variables, whereas the only RSG theoretical mass-loss prescription from Kee et al. (2021) hinges on knowledge of the turbulent velocity, which is barely constrained from observations and does not yet account for any radial or tangential change. Supported by almost a billion CPU hours at HPC facilities for theoretical modeling purposes and the provision of specialized computing facilities for data analysis, several groups are now collaborating with the aim to provide the community with improved mass-loss rate prescriptions accounting for this 3D binary perspective.

4.3.1. The red supergiant problem.

The preceding discussion will assist us in addressing the RSG problem, which concerns the question as to why the observed upper limit of ∼16 M$_\odot$ on the masses of Type IIP SN[6] progenitors appears to be significantly lower than the maximum mass of ∼30 M$_\odot$ for stars expected to explode while they are RSGs (Smartt et al. 2009). Numerous explanations have been considered including a steeper initial mass function (Smartt et al. 2009); the loss of the loosely bound hydrogen envelope of the most massive RSG stars prior to core collapse (Yoon & Cantiello 2010); the proposition that enhanced mass loss might limit the RSG mass to ∼20 M$_\odot$ (Groh et al. 2013); or the fact that massive stars collapse to black holes with optically dark or faint failed SNe (Woosley & Heger 2012). Another direction was to argue that for stars whose mass is greater than ∼15 M$_\odot$, the mass-loss rate should be higher than that currently considered in stellar evolution codes (Ekström et al. 2012); as cause for this increase in mass-loss rate, it was suggested that some of the most external layers of the stellar envelope might exceed the Eddington luminosity. Each of these explanations is grounded on uncertainties in the theoretical models, with the latter proposal by Ekström et al. (2012) seeming mutually incompatible with the conjecture formulated at the start of Section 4.3.

However, the puzzle that RSGs with masses of ∼16–30 M$_\odot$ have not been identified as progenitors of Type IIP SNe can also be examined from the perspective of retrieval analyses. An insufficient circumstellar dust correction for the pre-SN mass loss could bias the progenitor mass estimates to lower values (Walmswell & Eldridge 2012). Although the SED analysis of Walmswell & Eldridge (2012) was criticized by Kochanek et al. (2012), the underlying rationale can be reviewed in light of the scientific discourse embarked upon at the start of Section 4.3. Admittedly, the following discussion is narrowly confined to this one characteristic of retrieval modeling, and other potentially influential characteristics are not considered.

A first point of consideration deals with the binary hypothesis and the well-established issue that the binary fraction increases with stellar mass. The larger the stellar mass of the primary star, the larger the fraction of companions that will inspiral owing to the larger gravitational attraction by the primary star (Decin et al. 2020). For a binary system with a decreasing orbital distance, the EDE will become more pronounced. Higher densities in the EDE promote the formation of (crystalline) dust grains (Decin et al. 2019). Hence, it is to be expected that stars of higher initial mass can have a higher dust mass in their CSE, so the circumstellar dust correction is weighted higher in the final estimate of the pre-SN mass loss. A second manner of reasoning touches upon the issue of 3D clumps. Following the argument of Schwarzschild (1975), the size of the convection bubbles for stars of higher mass (and larger radius) will be larger. Using the same diameter-to-depth ratio of three as Schwarzschild (1975), this implies that the depth—and corresponding dust optical depth—might be larger for more massive stars so the impact of a proper circumstellar dust correction is larger. These assertions permit the extreme hypothesis that the RSG problem is potentially not so severe as currently considered, and the real solution can only be formulated under the condition of a detailed 3D analysis of the pre-SN mass loss. Of course, this is not a Solomon-like resolution but only one step in a holistic approach of tackling this dilemma. Recent studies even argue that the upper limit cut-off is likely to be higher and has large uncertainties ($M = 19^{+4}_{-2}$ M$_\odot$), implying that the statistical significance of the RSG problem is less than 2σ (Davies & Beasor 2020a,b).

<div style="float:right">

Eddington luminosity: maximum luminosity a star can achieve so that the outward radiation force balances the inward gravitational force

</div>

---

[6]Type II supernovae can be further subclassified into II-P (plateau light curves), II-L (linear decline light curves), IIn (narrow emission lines), and some peculiar events generically labeled II-pec.

4.3.2. Survival rate of (exo)planets.

The future of our own planet, the Earth, seems far from smooth sailing. Cogent modeling by Schröder & Smith (2008) suggests that the Earth will be swallowed by the time that the Sun is near its tip of the red giant branch (RGB) phase, ~7.6 Gyr from now. At that moment, the solar radius will reach ~1.2 AU, whereas Earth's orbit will hardly ever exceed 1 AU by a significant amount. This is caused by a competition in orbital widening induced by the solar RGB wind reducing the Sun's mass and orbital tightening owing to dynamical drag with the lower chromosphere and to orbital angular momentum loss due to tidal interaction with the giant Sun. Tidal interaction is dominant so the planet Earth cannot escape engulfment. Although not all parameters are invariably rigorously defined—in particular the tidal friction coefficient—it seems that doomsday is unavoidable. There is a future beyond the Sun's RGB evolution only for planets whose current orbital separation is greater than ~1.15 AU.

A larger RGB mass-loss rate would delay the engulfment and lead to smaller orbital separations for planets still able to survive. In their modeling approach, Schröder & Smith (2008) used an adapted form of Reimers' law (1975) to describe the cool wind—driven not by dust but presumably by (magneto)acoustic processes—that was physically motivated by a consideration of global chromospheric properties and wind energy requirements,

$$\dot{M} = 4 \times 10^{-13} \eta_{SC} \frac{L_\star R_\star}{M_\star} \left(\frac{T_{\text{eff}}}{4{,}000\,\text{K}} \right)^{3.5} \left(1 + \frac{g_\odot}{4{,}300\,g_\star} \right), \qquad 20.$$

with $\eta_{SC} = 0.2$ and $g_\odot$ the solar surface gravitational acceleration. Following Equation 20, the mass-loss rate of the giant Sun would be around 4×10^{-8} $M_\odot$ year^{-1} at the tip of the RGB. The feeble RGB mass loss is difficult to constrain from observations. The first detection of rotational CO line emission arising from an RGB wind was announced in 2014; the derived mass-loss rate is around a few 10^{-9} $M_\odot$ year^{-1} (Groenewegen 2014). A promising way to measure the RGB mass loss is to obtain a difference in stellar mass between two points in its evolution and use this to determine a scaling parameter such as η in Equation 1 or η_{SC} in Equation 20 (McDonald & Zijlstra 2015). This can be achieved in globular clusters, where one can probe the individual stars with accurately known distances, metallicities, abundances, and ages. Using 56 well-studied globular clusters, McDonald & Zijlstra (2015) derived as median values $\eta = 0.477 \pm 0.070$ and $\eta_{SC} = 0.172 \pm 0.024$, with very little metallicity dependence. This provides support to a Reimers-like law being a good RGB mass-loss model and to the model predictions of Schröder & Smith (2008).

Given the conjecture that AGB mass-loss rates for single stars or stars isolated from angular momentum deposition might be overestimated, the follow-up question then deals with the impact of that conjecture on the survival rate of planets. At first glance, this question might seem quite semantic, given the current lack of directly imaged planets in the close vicinity of cool aging stars and remembering the critical remark on that matter (see Section 4.1). But to quote the old maxim: "Absence of evidence is not evidence of absence." Given the large number of exoplanets currently detected and expected to be present in the Universe, and our current knowledge of stellar and planetary evolution, this inquiry on the survival potential of (exo)planets gets more substantial. For a reduced AGB and/or RSG mass-loss rate the predictions are, however, not at all auspicious because the change of orbital separation, da/dt, scales with the mass-loss rate. The lower mass-loss rate implies a lower rate of orbital widening, if occurring, and hence more (exo)planets experiencing a catastrophic encounter with their giant mother star due to tidal interaction. Therefore, escaping the doomsday scenario is more challenging than previously suggested.

5. THE THREE-DIMENSIONAL LIFE OF MOLECULES AND DUST GRAINS

To comprehend the essence of mass loss requires an understanding of the driving forces that dictate the nature of the phenomenon. Delving into the *why* question will provide feedback to the how question, and vice-versa. Our view of the essential processes has gradually been enriched thanks to the enormous capacities of modern telescopes and space observatories designed for optical, IR, and microwave investigations of cool astronomical objects. Furthermore, a new window for exploring dust formed in stellar outflows commenced in 1987 with the detection of small particles in the matrix material of certain meteorites that originated from stars whose lives ended before the formation of our Solar System: the presolar grains (Nittler & Ciesla 2016). Long before this detection, Cameron (1973, p. 545) speculated about "Interstellar grains in museums?" and concluded that primitive carbonaceous chondrites may harbor presolar grains, but it was Lewis et al. (1987, p. 160) who stated, "Interstellar dust contains diamonds" in the final phrase in the abstract of their paper in *Nature*. Before you consider any space exploration, the diamonds were tiny—i.e., only about ~ 10 Å.

This is where we reach the other spectrum of astrophysics, the regime in which the small pieces make up the big picture. These small pieces seldom bear any resemblance with smooth spherical particles, not even for the micrometer-sized dust grains (see **Figure 7**). For chemists, micrometer-sized dust grains are macroscopic. Even when staying within the realm of solid-state physics, it is well established that further size reduction from the macroscopic to length scales of only a few nanometers can lead to dramatic changes in a material's properties, including its atomic ordering, quantum, and surface effects (e.g., Lamiel-Garcia et al. 2017, Gobrecht et al. 2017). Wondering then how solid-state species form, we enter the world of atoms and molecules, which undergo a sequence of collisional association and recombination reactions to form polyatomic molecules of ever-increasing size, the gas-phase clusters (see **Figure 7** and the **Supplemental Text**). Under favorable conditions, the clusters condense and form the first dust seeds consisting of ten to several hundred atoms. The seed nuclei become the substrate to which molecules are added, resulting in further growth of the condensed phase, which eventually can reach the macroscopic regime. By the end of this process, the macroscopic dust species involve the accumulation of typically 10^6–10^9 atoms in a single grain.

5.1. Molecules and Dust Grains Identified in Stellar Outflows

Ground-based and space-borne observatories have been instrumental in detecting the fingerprints of the gas-phase and solid-state constituents of stellar outflows. Their identification was secured through confrontation with the outcomes of laboratory experiments and quantum-chemical calculations.

5.1.1. Molecules. Observatories that operate in the micrometer and millimeter-wave bands such as the *Infrared Space Observatory* (ISO), the James Clerk Maxwell Telescope, the IRAM 30-m telescope, the Plateau de Bure Interferometer (PdBI), and ALMA have boosted the detection of cosmic molecules via their rotational and vibration–rotation spectroscopic fingerprints. The wavelength resolution of most telescopes in the mid- and near-IR is moderate, $\Delta\lambda/\lambda \sim 10^{-4}$, compared with gas-phase spectra, whose frequencies can be determined to an accuracy of about 1 part in 10^7 or better in narrow line sources with heterodyne receivers on radio telescopes. In his excellent review, Olofsson (2005) provided a table listing the detection of 63 molecules in AGB winds. **Table 2** gives an update fifteen years later: Currently 105 molecules have been

Table 2   Molecules identified in the winds of cool evolved stars

2 atoms	AlCl	AlF	AlO	C_2	CN	CO
	CP	CS	FeO (?)	HCl	HF	KCl
	NO	NS	NaCl	OH	PN	PO
	SO	SiC	SiN	SiO	SiS	TiO
	VO					
3 atoms	AlNC	AlOH	C_2H	C_2S	C_3	CCN
	CCP	CO_2	CaNC	FeCN	H_2O	H_2S
	HCN	HCP	HNC	KCN	MgCN	MgNC
	NaCN	SO_2	SiC_2	SiCN	SiCSi	SiNC
	TiO_2					
4 atoms	c-C_3H	l-C_3H	C_2H_2	C_3N	C_3O	C_3S
	H_2CO	H_2CS	HC_2N	HMgNC	MgCCH	NCCP (?)
	NH_3	PH_3	SiC_3			
5 atoms	c-C_3H_2	C_4H	C_5	CH_2CN	CH_2NH	CH_4
	H_2CCC	HCCCN	HCCNC	HNC_3	MgC_3N	SiC_4
	SiH_4					
6 atoms	C_2H_4	C_5H	C_5N	C_5S	CH_3CN	H_2CCCC
	HC_4N	MgC_4H	SiH_3CN			
≥7 atoms	C_6H	C_7H	C_8H	CH_2CHCN	CH_3CCH	CH_3SiH_3
	H_2C_6	HC_5N	HC_7N	HC_9N	PAH	
Ions	C_3N^-	C_4H^-	C_5N^-	C_6H^-	C_8H^-	CN^-
	HCO^+					

Note: (?) indicates a tentative identification.

detected in stellar outflows. This is roughly 50% of all molecules discovered in outer space; the extensive review by McGuire (2018) lists 204 molecules, to which 6 other ones can be included ($MgCCH$, MgC_3N, MgC_4H, and CaNC, and potential detections of NCCP and FeO) (Agúndez et al. 2014; Cernicharo et al. 2019a, 2019b; Decin et al. 2018a). I opted to include in **Table 2** the polycyclic aromatic hydrocarbon (PAH) molecules because their characteristic C–H and C–C stretching and bending modes have been detected in AGB stars (Boersma et al. 2006, Smolders et al. 2010), although the precise carriers have not been determined.

In addition, there is the obvious difference between being and seeing. Given the current detections, our knowledge of quantum-chemical selection rules, reaction kinetics, and the thermodynamical wind properties, we have no doubt about the presence of some molecular species, but they remain hidden from our telescopes. The most obvious and important example is molecular hydrogen, H_2, the most abundant molecule in stellar winds. This nonpolar light molecule has no permanent electric dipole moment and is not easily observed under the conditions prevalent in AGB CSEs. However, H_2 is detected in 2-μm spectra of AGB variables (Hinkle et al. 2000), but it is not always straightforward to determine whether an IR line has a circumstellar origin or whether it emerges from the (extended) atmosphere. The same argument holds for other molecules such as CH (Matsuura et al. 2007).

Of the 105 molecules listed in **Table 2**, only 27 do not contain carbon and most are diatomic species. This is due to the reactive nature and unique bonding properties of the carbon atom, but also because the nearest ($D \sim 150$ pc) and best-known carbon star, CW Leo, has a high mass-loss rate ($\dot{M} \sim 1.5 \times 10^{-5}$ $M_\odot$ year^{-1}; De Beck et al. 2012, Cernicharo et al. 2015). Just for comparison, the nearest O-rich AGB star, R Dor, resides at a distance of $\sim$59 pc and has a mass-loss rate of

only $\sim 1.5 \times 10^{-7}$ M$_\odot$ year^{-1} (Danilovich et al. 2016), whereas the O-rich supergiant VY CMa has an enormous mass-loss rate of $\sim 2 \times 10^{-4}$ M$_\odot$ year^{-1}, but resides at a distance of $\sim 1,150$ pc (Decin et al. 2006, Zhang et al. 2012).

In all CSEs, the dominant molecule apart from H$_2$ is CO, which forms at local thermodynamic equilibrium (LTE) in the stellar photosphere and consumes all of the remaining atomic C or O—i.e., whichever is the least abundant of the two. (See the sidebar titled Carbon- and Oxygen-Rich Cool Stars.) For a long time, it was therefore thought that O-rich winds are very deficient in other carbon-bearing molecules, whereas C-rich ones were believed deficient in other oxygen-bearing molecules, but this picture has gradually been amended. First of all, there was the detection of HCN, HNC, and CS in O-rich CSEs, which were explained on the assumption of an active photochemistry in the outer CSE layers owing to the penetration of harsh interstellar UV photons (Bujarrabal et al. 1994). Although this process can explain the formation of atypical molecules in the outer envelope, it cannot resolve the unanticipated detection of CO$_2$ in the inner wind of O-rich AGB stars and H$_2$O, OH, H$_2$CO, and SiO in carbon-rich winds (Justtanont et al. 1998; Ryde et al. 1998; Melnick et al. 2001; Ford et al. 2003, 2004; Schöier et al. 2006, 2013; Decin et al. 2008; Velilla Prieto et al. 2015). Little by little, it has become clear that we should abandon the convenient idea of LTE; we need to acknowledge that the chemistry is more complex than what is inferred by the assumption of TE and instead is best described as nonequilibrium chemistry. I say "little by little" because that change in mindset didn't happen silently and overnight. It was not that there was a disregard of unwelcome evidence, but nonequilibrium calculations imply solving the full set of rate equations for the detailed reaction kinetics in the rapidly expanding and cooling gas. These calculations are not only CPU expensive; the challenge here is also to know the rate coefficients, which commonly depend on the temperature and often also on the gas density or on external sources such as the ISM radiation field or cosmic rays. Not only can chemical reactions relevant for astrophysics rarely be extracted from industrial resources but, in addition, the gas number densities in CSEs are generally lower than in the laboratory by ten decades. One should also realize that only $\sim 15\%$ of the reaction rates listed in astrochemical databases are experimentally obtained at room temperature (~ 300 K), only $\sim 2\%$ have rate constants at temperatures below 200 K, and less than 0.5% have rate constants at temperatures below 100 K. For some reaction rates, the results of theoretical quantum-chemical calculations are available. However, the complexity of the electronic structures often complicates a reliable theoretical prediction of the rate coefficients. Accurate rates are particularly critical for the rate-limiting steps (see Section 5.3.1).

Photoinduced processes in the outer CSE are not the only cause for out-of-equilibrium chemistry. In general, the low particle densities in CSEs imply that reaction conditions can change considerably before a reaction has run to completion; a particular example is the extended atmosphere, which is subject to pulsation-induced shocks (Cherchneff 2011, Gobrecht et al. 2016). In addition, the material is subject to chromospheric UV fields (notably for RSG stars) and ionizing radiation from decaying radioactive nuclei. We now think that photoinduced processes are particularly relevant in dictating the outer-envelope chemistry: Given the fact that contemporary observations reveal the envelopes to be nonhomogeneous (see Section 3), recent theoretical models incorporating the emergence of 3D clumps indicate an enhanced penetration depth of interstellar photons resulting in a vast difference in predicted molecular abundance structures compared with the smooth envelope case (Agúndez et al. 2010, Van de Sande et al. 2018b, Van de Sande & Millar 2019).

In addition, we can get an extra glimpse of the molecular content of the winds of AGB stars by studying the circumstellar environment of their immediate successors, the young post-AGB stars, in which the increased UV flux and the presence of shocks can affect the chemistry. Good examples

NUCLEATION

Gas does not spontaneously go over to the solid bulk phase because there exists an energy barrier between the metastable and stable phases that makes a global phase change highly improbable. An energetically more favorable pathway is the formation of nano-to-microscale density transition nuclei, called the cluster model of the nucleation process. During this process, atoms and molecules undergo a sequence of collisional association reactions to form polyatomic molecules of ever-increasing size. Clusters are generally represented by the symbol M_N, which is an assemblage of a (small) number N of atoms or molecules, denoted here as monomer M. Obviously, the term small is ambiguous, and distinguishing between a small gas-phase cluster and a larger particle can be difficult. A common practice is to define a small cluster as a system that still has a discrete electronic structure (as in an atom), and therefore differs from a larger system that has electronic bands. The properties of clusters, including optical, electronic, magnetic, and chemical properties, change drastically with their size. Generally, nucleation is a very inefficient process, and only a small fraction of the collisions between the gas phase atom or molecule and a small cluster will lead to cluster growth.

include the envelopes of the C-rich objects AFGL 618 and AFGL 2688 and the O-rich object OH 231.8+4.2, in which molecules such as H_2, OCS, HNCO, HNCS, CH_3OH, H_3O^+, SO^+, CO^+, CH^+, N_2H^+, H_2CO, HC_4H, HC_6H, CH_3C_2H, CH_3C_4H, and C_6H_6 have been detected.

These molecules and atoms form the building blocks of the solid-state species that can form if density and temperature are of the right order for dust formation to take place. The process of solidification is modeled under the common interpretive framework of nucleation, a process during which the nano-to-microscale transition of nuclei form; see also Section 5.3. (See the sidebar titled Nucleation.)

5.1.2. Condensates. Condensates are characterized by their mineralogical structure (monocrystalline, polycrystalline, or amorphous), their chemical composition (homogeneous, but most often heterogeneous and layered), and their geometric shape. In contrast to molecules, the analysis of IR dust spectral features does not always provide sufficient insight into the mineralogical, chemical, and geometric properties. This stems from the fact that dust spectral features often originate in radiatively excited functional groups of atoms constituting the grain, such as the stretching vibration of the Si–O bond (around 9.5 μm) and the bending vibrations of the O–Si–O group (around 18.5 μm) within the SiO_4 tetrahedron of silicates. As such, it is often impossible to unequivocally determine the exact grain properties from the analysis of IR spectra because, for example, two different amorphous silicate-type grains can each display the broad emission pattern in their mass absorption coefficient around 9.5 and 18.5 μm (Jaeger et al. 1998, Molster et al. 2002). This is also the reason why the PAH molecules are sometimes analyzed in a way similar to that of dust species, because also for these macroscopic PAHs we witness the behavior of the functional C–H and C–C groups.

In particular, the ISO was ground-breaking for detecting new dust species (Tielens et al. 1998, Waters et al. 2000, Henning 2010); an overview of the dust grains identified in the winds of AGB and RSG stars can be found in **Table 3**. Instruments such as the ESO VLTI-MIDI (Very Large Telescope Interferometer–Mid-infrared Interferometric instrument) and VLT-SPHERE (Very Large Telescope–Spectro-Polarimetric High-contrast Exoplanet REsearch) interferometers were crucial for determining the location of the grains (Ohnaka et al. 2006, Norris et al. 2012, Karovicova et al. 2013). In this context, a very interesting yet unexpected discovery was the spectroscopic identification of pure crystalline silicate grains (pure forsterite, Mg_2SiO_4, and

Table 3 Condensates identified in the winds of cool evolved stars

Species	Formula	Species	Formula
Alumina	Al_2O_3	Diopside	$MgCaSi_2O_6$
Olivine	$Mg_{(2-2x)}Fe_{2x}SiO_4$	Water ice	H_2O
Pyroxene	$Mg_{(1-x)}Fe_xSiO_3$	Metallic Fe	Fe
Melilite	$Ca_2Al_2SiO_7$	Carbon	C
Magnesiowüstite	$Mg_xFe_{(1-x)}O$	Silicon carbide	SiC
Spinel	$MgAl_2O_4$	Magnesium sulfide	MgS
Silica	SiO_2	Hibonite	$CaAl_{12}O_{19}$
Titanium oxide	TiO_2	Titanium carbide	TiC

Note: More detailed information can be found in **Supplemental Tables 1** and **2**.

enstatite, $MgSiO_3$, the Mg-rich end members of olivine and pyroxene; Molster et al. 2002). Given an expanding and cooling envelope, grains are predicted to be amorphous and additional processes were sought for a further crystallization of the grains (see also Section 5.2). Some low-temperature crystallization process of unknown origin acting in circumstellar disks has been proposed (Molster et al. 1999b). However, our recent finding that the majority of cool aging stars with a measurable mass-loss rate might not live their lives alone but have a companion offers an alternative explanation (Section 4): In O-rich winds with low wind acceleration properties the companion can quite easily induce the formation of an EDE (El Mellah et al. 2020), which offers the perfect conditions for amorphous grains to be annealed into crystalline minerals owing to shock formation with an associated increase in temperature in the orbital plane (Decin et al. 2019).

What is really fascinating is that physical samples of these dust grains can be assembled here on Earth: These microscopic stardust grains are found in meteorites (see **Figure 7**). After their journey through the ISM, these grains survived the formation of the Solar System, where they were trapped inside asteroids, the parent bodies of the meteorites. These presolar grains have isotopic compositions indicating an AGB or RSG origin (Lodders & Amari 2005, Nittler et al. 2008, Davis 2011, Nittler & Ciesla 2016). A common property is that they are chemically stable and for this reason have survived their journey to Earth. The grain's morphology, mineralogy, and composition reflect the formation conditions in the CSE, and hence complement the studies of the IR spectral bands. The cosmochemical studies of these extraterrestrial rocks even allowed the identification of AGB and RSG dust grains that escape identification via IR spectral features (see **Supplemental Table 2**). Typical grain sizes range from a few nanometers to 1 μm (Goderis et al. 2016). One should realize, however, that the laboratory techniques induce a bias in species detected due to the fact that some species might be dissolved out during the preparation process. In addition, smaller grains are more difficult to detect, resulting in a grain size bias.

5.2. Challenging the *why* Question

The wealth of observations has guided the theoretical models and conveys the principles to which the models must adhere. The ISO observations of circumstellar dust around AGB stars have been interpreted within the context of TE condensation sequences (Onaka et al. 1989, Tielens et al. 1998). Gearing the discussion toward oxygen-rich environments, the silicate thermodynamic condensation sequence predicts two branches to occur (Grossman & Larimer 1974, Tielens 1990). The condensation sequence starts with that of Al_2O_3 (around 1,700 K). Gas-solid reactions lead to the formation of the first silicates, melilite ($Ca_2Al_2SiO_7$) and diopside ($CaMgSi_2O_6$), around

1,500 K. Most of the silicon will condense out in the form of pure Mg-rich silicates, first forsterite (Mg_2SiO_4, around 1,440 K) and later enstatite ($MgSiO_3$). Finally, reactions with gaseous iron will convert some enstatite into fayalite (Fe_2SiO_4) at about 1,100 K.

Observations indicate a very low Fe/Mg content of crystalline silicates (Fe < 10%; Molster et al. 1999a). This can be explained in a scenario proposed by Tielens et al. (1998) in which crystalline Mg-rich silicates form close to the photosphere. These grains are thermally coupled to the gas via collisions and attain temperatures well above the glass temperature (of ~1,050 K), resulting in a crystalline structure. Upon the expansion and cooling of the gas, it becomes possible for Fe to be gradually incorporated in the silicate grains. The inclusion of Fe results in a considerable increase in the near-IR absorption coefficient so that just enough Fe can be incorporated for the radiative temperature of the grain to remain below the sublimation temperature of around 800–1,100 K with an Fe inclusion of around 20%. However, at these low temperatures the Fe-rich lattice cannot reach its energetically most favorable structure that leads to the formation of amorphous Fe-rich silicates. The Fe-rich silicates efficiently absorb the stellar light in the near-IR so that the radiation pressure on the grains becomes large enough to initiate a stellar wind. The scenario proposed by Tielens et al. (1998) rests on an important conjecture, namely that efficient dust nucleation and growth actually take place close to the stellar photosphere. As discussed by Tielens (1990), this is far from obvious not only because the densities have to be high ($n \gtrsim 10^{13}$ cm^{-3}) for efficient nucleation but also because there is a lack of stable monomers.

Given the observations, thermodynamics seemed to be well obeyed, if one accounts for the freezing-out of chemical reactions that occurs when the density and temperature are too low and chemical reactions cease (Tielens et al. 1998). In this way, the macroscopic world of dust grains was handled under the convenient assumption of TE. If so, one should not care about the exact pathway of dust condensation because the most stable condensates will form under the general temperature–pressure conditions and relevant element mixtures. One can compare it with the analogy of a ball rolling down a—rather smooth—hill: The ball will come to rest in the valley independent of the path taken. So, the TE principles provided an answer to the *why* question.

A striking disruption of this comfortable interpretation occurred in 2006, when Woitke applied an elegant deduction—by essentially solving Equations 4 and 6—to prove that the qualitative scenario proposed by Tielens et al. (1998) for the wind driving in O-rich AGB stars actually does not hold (Woitke 2006b). In addition, through the adoption of detailed RHD models, Woitke showed that, in fact, two dust layers are formed, an almost pure glassy Al_2O_3 layer close to the star and a more opaque Fe-poor Mg-Fe-silicate layer farther out. However, because only a small fraction of Fe can be incorporated in the silicate grains, because otherwise they become too hot, almost no mass loss occurred ($\dot{M} \lesssim 10^{-10}$ M$_\odot$ year^{-1}). This paper not only reopened the quest for the driving mechanism of O-rich AGB winds but also touched on the fundamental *why* question.

Various solutions have been offered to solve this dilemma. Höfner & Andersen (2007) provided an unorthodox suggestion—their words—involving the formation of both carbon and silicate grains. This scenario implies departures from CE, because a fraction of the carbon is not bound in gaseous CO but is available for grain formation. One year later, Höfner (2008) provided an alternative mechanism in which the Fe-free grains can grow to sizes large enough (~200 nm– 1 μm) close to the star for photon scattering to compensate for their low near-IR absorption cross-sections and to trigger the onset of a stellar wind. Recent VLT-NACO [Very Large Telescope– Nasmyth Adaptive Optics System (NAOS)-Near-Infrared Imager and Spectrograph (CONICA)] and SPHERE data support the presence of large transparent grains (~0.3 μm) at a distance of ~0.5 $R_\star$ in some AGB stars (Norris et al. 2012, Khouri et al. 2016), but these data cannot pinpoint the chemical composition of the grains. The current line of reasoning stipulates that Al_2O_3

grains can grow around ~0.5 $R_\star$ from the star and reside there in a gravitationally bound dust shell (Khouri et al. 2015, Höfner et al. 2016, Höfner & Freytag 2019). Once the temperature gets below ~1,200 K (around 4 $R_\star$), silicates can form as a mantle around the aluminum-oxide cores. For grain sizes above ~100 nm, a dust-driven outflow can be expected owing to the operation of scattering.

Each of the proposed solutions is, however, a macroscopic solution and bypasses the question of the molecular formation routes toward the predicted grain types. Although Höfner & Andersen (2007) suggested a nonequilibrium formation route for carbon grains, they did not present a detailed non-CE study, and the abundance of available carbon was a parameter in the models. In the same vein, most modern RHD wind models for O-rich AGB winds assume the first dust seeds are present, after which further growth to micrometer-sized dust grains can take place (Höfner & Olofsson 2018). Hence, the conjecture posed by Tielens (1990) is still open some thirty years later: We still assume in the models that efficient dust nucleation occurs close to the star, although we now acknowledge the shortcomings of TE to understand dust nucleation.

Leaving behind the comfortable landscape of TE, one enters a new gigantic playground in which the rules of the game are not always very clear, and sometimes even undefined. Given the earlier discussion on the challenges of gas-phase chemical kinetics (Section 5.1), it is to be acknowledged that a proper description of dust nucleation is a fundamentally unattainable endeavor. The reaction rate coefficients entering the description of cluster growth are often unknown, and the knowledge of the geometric configurations of the energetically low-lying structures is often lacking (Bromley et al. 2016; Gobrecht et al. 2017, 2018; Boulangier et al. 2019). The same applies to the description of grain growth and destruction in which case the adsorption and desorption coefficients are often only approximately known because the atomistic details of this process are unknown (Cuppen et al. 2017). In aiming to answer the *why* question, we have to enter this kinetics playground. Unlike the situation of TE, for which the path is unimportant, an understanding of the path(s) taken toward dust nucleation will be central in our quest. In fact, this addition of specific paths implies an important change in the topology of the landscape. In TE, the topology is convergent toward the most stable solutions, the thermodynamic sink. Turned around, this convergent TE solution in the forward direction becomes divergent in the backward direction, prohibiting one from going back in time and addressing the *why* question. Complicating the situation in a non-CE sense implies that we move away from this forward convergent–backward divergent topology and that we can seek the real roots of mass loss.

5.3. Dust Nucleation: Top-Down Versus Bottom-Up

The realistic description of dust formation and growth requires a treatment based on reaction kinetics, which is practically impossible because it would require the solution of a set of order 10^9 rate equations for which most of the reaction rate coefficients are unknown and potentially not even critical. This task is considerably simplified by applying a two-step process in which, first, suitable seed particles have to form from the gas phase (the nucleation process; see the sidebar titled Nucleation), and in a second step, the seed nuclei form the substrate to which molecules are added (Gail & Sedlmayr 2013). During the past decade, we have witnessed considerable progress in our understanding of the formation of the first seed nuclei using first principles, i.e., following a bottom-up approach. After delving through this section, however, the reader will realize that the situation is still far from satisfactory.

5.3.1. Some theoretical aspects.
Various levels of theory exist for the description of nucleation. One can broadly classify them as the top-down and bottom-up approaches, with some variants in
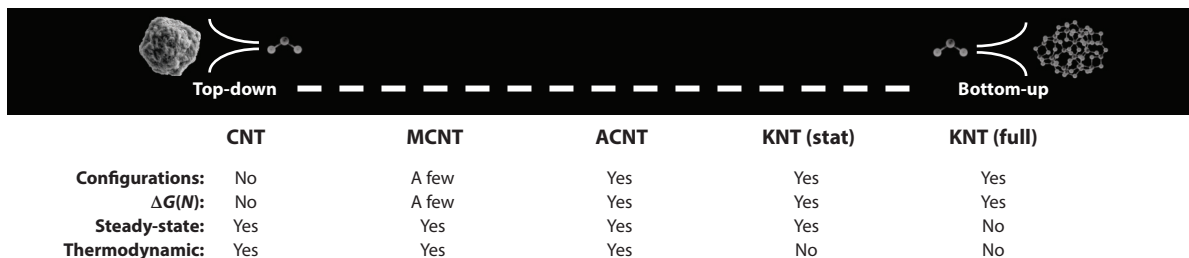
	CNT	MCNT	ACNT	KNT (stat)	KNT (full)
Configurations:	No	A few	Yes	Yes	Yes
$\Delta G(N)$:	No	A few	Yes	Yes	Yes
Steady-state:	Yes	Yes	Yes	Yes	No
Thermodynamic:	Yes	Yes	Yes	No	No

Figure 10

Schematic representation of the different levels of theory used for the calculation of the nucleation rate. The different approaches (from top-down to bottom-up) include the classical nucleation theory (CNT), the modified classical nucleation theory (MCNT), the atomistic classical nucleation theory (ACNT), and the kinetic nucleation theory (KNT). Within KNT, the full time-resolved kinetic model can be solved (full) or a stationary approach can be pursued [$d(n, t)/dt = 0$; stat]. The different rows indicate if ground-state configurations are calculated using density functional theory (DFT), including the calculation of $\Delta G(N)$, if the nucleation rate is calculated under the assumption of steady state, and if thermodynamic quantities are needed—in which case "no" indicates that the nucleation rate can in principle be calculated without recourse to these quantities, although rarely are all rate efficiencies available for this situation to occur.

between; a schematized representation is shown in **Figure 10**. In order to understand the challenges in this field, I have summarized the main principles behind the various approaches in the **Supplemental Text**. The key points for consideration are summarized here. Before doing so, a general note is appropriate. The term nonequilibrium chemistry, so frequently used in the literature, may convey some information but is devoid of specific information. Only when delving through the detailed mathematical derivations does it often become clear which physical quantity is not adhering to an equilibrium condition.

The challenge of the bottom-up approach is that one needs the geometric configurations with the lowest potential energy (i.e., the global minima) and their respective binding energies for each cluster of size N forming along the pathway toward the macroscopic solid compound. In a first step, one determines a good approximation of the geometric configuration of the molecular clusters by searching the potential energy surfaces for the increasingly complex space of possible arrangements. This first step can already be quite CPU demanding. The candidate configurations are then used as the initial configurations in density functional theory (DFT) calculations to find the lowest-energy structures. (See the sidebar titled Density Functional Theory.) For these structures, the thermodynamic properties (entropy, enthalpy of formation $\Delta_f H$, and the Gibbs free energy of formation $\Delta_f G$ are then computed; the Gibbs free energies of formation are then used to calculate $\Delta G(N)$, which is the free energy change associated with the formation of a cluster of size N from the saturated vapor. Using the most modern quantum chemical codes, the DFT method currently allows systems containing some 50 atoms to be calculated (Gobrecht et al. 2018). Owing to the computational challenges, only a few systems of relevance for astrophysical research have been computed at this level of theory; notable examples include $(SiO)_N$ ($N = 1$–20; Bromley et al. 2016), $(TiO_2)_N$ ($N = 1$–38; Jeong et al. 2000, Lee et al. 2015, Lamiel-Garcia et al. 2017, Boulangier et al. 2019), $(C)_N$ ($N = 1$–99; Mauney et al. 2015), $(Al_2O_3)_N$ ($N = 1$–8; Li & Cheng 2012, Gobrecht et al. 2018, Boulangier et al. 2019), and $(MgO)_N$ ($N = 1$–10; Chen et al. 2014, Boulangier et al. 2019), with each of them being proposed as dust precursor candidates in stellar winds.

Given the general lack of quantum chemical data on the cluster properties, various simplifications have been pursued along the path (see **Figure 10**). In CNT, one uses the capillary approximation to represent the potentially unknown $\Delta G(N)$ via the surface tension of the bulk material, σ_∞ (see the **Supplemental Text, Equation S40**). This approximation is only valid for $N \gg 1$ and is also based on the assumption of thermal and chemical equilibrium. It also bypasses the

Binding energies: energy required to separate constituent atoms and/or molecules from a system of particles

Gibbs free energy (ΔG): part of the heat of a reaction that can be converted to useful work

DENSITY FUNCTIONAL THEORY

To derive the cluster configurations, one needs to solve the Hamiltonian of a system of N_e interacting electrons and fixed nuclei for the many-body eigenstate Ψ_k, $H|\Psi_k\rangle = E_k|\Psi_k\rangle$. Here, H denotes the Hamiltonian, E_k the energy of the system, and Ψ_k the wave function. The basis for density functional theory (DFT) is the Hohenberg–Kohn theorem (Hohenberg & Kohn 1964), which states that the ground-state energy for an electronic system is a functional of the electron density. Hence, in DFT calculations, the electron density rather than the wave function is used to describe the system. This reduces the dimensions of the system drastically, from $3N_e$ variables to only 3, the three spatial coordinates. As a result of the Hohenberg–Kohn theorems, the ground-state energy functional $E[n]$ is stationary with respect to the number density n. Determination of the ground-state number density $n_0(\mathbf{r})$ is then a solution to the constrained variational equation,

$$\frac{\delta}{\delta n(\mathbf{r})}\left[E[n(\mathbf{r})] - \Lambda\left(\int d\mathbf{r}\, n(\mathbf{r}) - N_e\right)\right] = 0,$$

with $\mathbf{r}$ the space coordinate and Λ the mathematical variable Lagrange multiplier (Kristyan 2013).

well-known fact that at the nanoscale quantum effects become important, causing the nano-sized particles to behave very differently from their bulk counterpart. MCNT aims to improve CNT by linking the macroscopic solid bulk and microscopic cluster properties. Using DFT, the cluster properties of a few of the smallest clusters are calculated. The derived $\Delta G(N)/N$ values are then fitted using an analytical formula (see the **Supplemental Text, Equation S51**) to allow extrapolation to larger values of N. That way, one accounts for the curvature of the small clusters. For values of $N \to 1$, the atomistic version (ACNT) is recommended, in which the binding energies as calculated from DFT are explicitly used (see the **Supplemental Text, Equation S56**).

In the full time-resolved kinetic model, one solves the full time-dependent set of coupled ordinary differential equations describing the rates of change in number density of each cluster of size N, $dn(N, t)/dt$; see the **Supplemental Text, Equation S28**. If the reaction efficiencies are known, the growth and evaporation timescale can be calculated directly, without additional need of the thermodynamic quantities. However, the growth efficiencies are often uncertain, and the evaporation efficiencies are mostly unknown. Therefore, methods have been developed based on kinetic nucleation theory (KNT) and thermodynamic arguments (see the **Supplemental Text**). Within KNT, CNT, MCNT, and ACNT, it is possible to formulate the stationary nucleation rate, $J_\star(t)$, assuming that the cluster densities remain constant over time, i.e., $dn(N, t)/dt = 0$. Assuming that the growth of clusters only occurs via monomer addition within the context of homogeneous nucleation, $J_\star(t)$ can be written as

$$J_\star(t) \simeq z(N_\star) f(N_\star, t)\, \mathring{n}(N_\star), \qquad\qquad 21.$$

where $\mathring{n}(N)$ is the equilibrium density of a cluster of size N, and $f(N, t)$ is the monomer attachment rate (see the **Supplemental Text, Equations S38 and S46**). In the framework of CNT, MCNT, and ACNT, z is the kinetic Zel'dovich factor that takes a different value for each level of theory (see the **Supplemental Text, Equations S49, S52, and S59**), but $z = 1$ within KNT. $N_\star$ is the critical cluster size at which $\mathring{n}$ reaches its absolute minimum. The growth reaction of this cluster of size $N_\star$ is the bottleneck of the chemical network and, hence, is the rate limiting step.

For each level of theory, in addition one needs reaction rate coefficients for the calculation of attachment rate $f(N, t)$. One of the most detailed methods (used in astrophysical research) is based on the Rice–Ramsperger–Kassel–Markus (RRKM) theory of chemical activity, employing

a solution of the master equation based on the inverse Laplace transform method (in the case of $(SiO)_N$; Bromley et al. 2016). In the absence of accurate reaction rates, the rate can be approximated by using the geometrical cross-section and the Maxwell–Boltzmann distribution, so that

$$k = \pi (r_a + r_b)^2 \sqrt{\frac{8kT}{\pi \mu}} \left(1 + \frac{E_a}{kT}\right) \exp\left(-\frac{E_a}{kT}\right), \qquad 22.$$

with r_a and r_b being the radii of the colliding species, μ the reduced mass of the system, and E_a the activation energy, which is assumed to be zero if unknown (Boulangier et al. 2019). When dealing with large clusters $N \gg 1$, this reaction rate is often denoted as the sticking coefficient γ—i.e., the probability that an incoming monomer binds to the target cluster. Although in principle it can differ from unity, it is a customary assumption in classical nucleation theory (i.e., CNT, MCNT, and ACNT) to assume $\gamma = 1$.

5.3.2. Recent theoretical outcomes.

Given these various levels of theory, one wonders if taking the bottom-up directive of full kinetic modeling is like taking a sledgehammer to crack a nut. The nucleation process can, *mutatis mutandis*, be modeled using CNT, the theory that is currently most often used in astrophysical problems. Only a few authors address a comparison between the different approaches (Jeong et al. 2003, Goumans & Bromley 2012, Mauney et al. 2015, Bromley et al. 2016, Lee et al. 2018). These outcomes are summarized, in a somewhat encyclopedic way, in the **Supplemental Text, Section S3.5**. Before jumping to the bottom line of these comparisons, it is important to realize that each answer given should be interpreted within the context of the particular thermodynamical properties of the medium modeled.

Given the discussion in the **Supplemental Text, Section S3.5**, it seems that resorting to ACNT is sufficient to study dust nucleation in stellar outflows. On the condition that large enough N are reached in the DFT calculations, ACNT yields a fast method to compute the stationary nucleation rate. The only concern then is whether steady state is reached in the pulsation-dominated region where dust nucleation is thought to occur. This point has been addressed by Boulangier et al. (2019), who developed a full kinetic model to study the nucleation of $(TiO_2)_N$, $(SiO)_N$, $(MgO)_N$, and $(Al_2O_3)_N$ in O-rich AGB CSEs. Furthermore, they extended the model by including not only monomer interaction but also polymer interaction. Their results show that cluster growth is time dependent, but for some species the largest clusters are formed in only a few hours, whereas others take more than $\sim$50 days—i.e., a significant fraction of the AGB and/or RSG pulsation period during which the thermodynamic properties can change drastically.

Assuming the monomers are present, the full kinetic models of Boulangier et al. (2019) favor Al_2O_3 as the primary dust precursor candidate owing to the high temperature at which nucleation can occur ($\sim$1,800 K). However, if one starts from an atomic mixture, an acute problem arises because the concentration of the Al_2O_3 monomer is almost negligible in the relevant temperature range, and most of the aluminum is in the atomic form. These results suggest that among the possible candidates, TiO_2 clusters are the only possible dust precursors. However, the kinetic temperature corresponding to the spatial regions where dust is found is roughly 1,500–2,000 K (Norris et al. 2012, Khouri et al. 2016), well above the formation temperature of $(TiO_2)_N = 10$, which is around 1,000–1,200 K. Furthermore, a significantly larger fraction of presolar grains of AGB origin contain Al_2O_3 rather than TiO_2 grains (Choi et al. 1998, Stroud et al. 2004, Bose et al. 2010), although the expected smaller size of TiO_2 grains makes them more difficult to detect. So, alternative routes are now being explored to determine whether larger $(Al_2O_3)_n$ clusters can form bypassing the monomer, and using, for example, the $(Al_2O_3)_2$ dimer as the main building block, where the dimer is formed from oxidation reactions of the abundant Al_2O_2 molecule with AlO,

AlOH, OH, and H_2O (D. Gobrecht, J. Plane, and L. Decin, in preparation). Another possibility might be that large clusters can exist at higher kinetic temperatures than currently suggested by the model calculations, because of thermo-ionic electron emission (Demyk et al. 2004), or possibly radiative cooling (potentially via recurrent fluorescence or vibrational radiative cooling) rather than dissociating. The Nobel Prize–winning physicist Richard Feynman (1959) famously used as the title of his talk presented to the American Physical Society in Pasadena on December 29, 1959, *There's Plenty of Room at the Bottom*. This statement remains a stellar example of physics prognostication; much of that room has yet to be explored.

5.4. Discover the Path by Tracing the Route

So, this is where we are. In 2021, we still remain in the realm of the argument formulated by Tielens in 1990, and this despite considerable progress in observations, theoretical models, quantum chemical calculations, and laboratory experiments. The non-CE path followed during dust formation in O-rich environments has still not been identified. The path leading from bottom to top is not merely conceptual—i.e., a *gedanken* experiment—but rather it is a genuine path that the chemical system adheres to. It is the topology invoked by that path that allows us to reverse the time axis. And actually, we do not need to discover dozens of paths; just one is sufficient since the winner takes it all: If for a given chemical mixture several reaction chains lead to different condensation products, then the reaction chain with the highest nucleation rate wins. Once seeds of one kind start to form, other thermally stable materials will condense on the surface of these seeds, rather than forming seeds themselves. One might question if the quest for this path is too ambitious a target. My answer to this question is no. Thanks to the impressive increase in HPC facilities, it appears we have the beginnings of a solution to this tantalizing problem. And although nature is allowed the prerogative of thinking out of the box, even the conventional methods have only been vaguely explored. We have a few indications on the complex quantum chemical route map, but divergent thinking might be needed to identify the correct direction. I use the words "divergent thinking" because of the huge clumps of dust that are detected in the close vicinity of RSG stars (Cannon et al. 2021): Circumstances are far from ideal for dust to form under conditions of chromospheric and pulsation activity in a low-density region, but far from optimal is clearly not a synonym for impossible. Rather like extremophiles on Earth are an indication that life is not vulnerable but persistent, the same seems to hold for dust nucleation.

Quantum chemical calculations will help astronomers to discover the path to a new take on understanding circumstellar chemistry, which was recently launched with the ambitious *Stardust* project (**https://nanocosmos.iff.csic.es/**). By building a novel ultrahigh vacuum machine combining atomic gas aggregation with in situ characterization techniques, the aim is to reproduce and characterize the bottom-up dust formation process under conditions similar to those of evolved stars. The prime focus of the project is currently on carbon chemistry. By feeding the reactions with individual C atoms and H_2 molecules, it recently has been shown that aromatic species and fullerenes do not form efficiently under these conditions (Martínez et al. 2020). Furthermore, surface reactions can be studied with *Stardust*. This reveals that reactions on surfaces can process the deposited material and lead to the formation of aromatic systems (in this case benzene, C_6H_6, and naphthalene, $C_{10}H_6$, one of the smallest PAHs), similar to what might be happening in CSEs. However, it should also be noted that the results of Martínez et al. (2020) do not rule out gasphase pathways for forming aromatic molecules. Although one can conclude from experimental results subject to restricted conditions which reactions are possible, it is logically unsound to conclude which reactions are not possible, particularly over a time span of millions of years within

an environment in which temperature and density change by orders of magnitude. The phrase by Charles Dickens (1837) in his first novel *The Pickwick Papers* is particularly apt: "never say never."

Furthermore, current observational techniques allow one to tackle the problem from an empirical perspective. We are at an important point of history and are now able to spatially resolve the surfaces of stars other than the Sun and to follow the change of the 3D structures through time and, hence, gain access to an incredible amount of detail in a 4D spacetime. For example, using ALMA, we can follow the change in the radial abundance structure of molecules thought to be the building blocks of dust grains (TiO, TiO_2, SiO, AlO, and AlOH; Kamiński et al. 2017, Decin et al. 2017, Danilovich et al. 2020) to constrain the fraction of molecules left after dust formation. The challenges here are situated in (*a*) the lack of collisional rates for the species under study, (*b*) the need of radiative excitation rates (Einstein A-coefficients) for highly excited states, and (*c*) the nonspherical and time-varying geometry of the stellar winds (Danilovich et al. 2020). But again, these challenges are within reach thanks to modern HPC facilities. In collaboration with software engineers, we are on the verge of developing highly efficient algorithms for analyzing these data (de Mijolla et al. 2019; De Ceuster et al. 2020a,b). The ALMA observatory is not the only one to offer some resolution on this issue. The strongest constraints are obtained from a multiwavelength, multi-instrument setup allowing for contemporaneous observations, a strategy increasingly endorsed by intergovernmental organizations in astronomy. How else would we be able to explain the great dimming of Betelgeuse, the famous RSG in the constellation of Orion that is visible with the naked eye and that started fading in December 2019? Not only astronomers but also the broad public[7] were wondering if Betelgeuse's dimming meant it was about to explode. Like all RSGs, Betelgeuse will one day go SN. One of the currently most favored working hypotheses for this dimming is the ejection or instant formation of a huge dust clump (Cotton et al. 2020, Safonov et al. 2020, Montargès et al. 2021); again the seemingly impossible becomes possible, although this might not be exactly what the public has hoped for. The principle by which dust clouds arise turns out to be extraordinarily effective but still obscure. It is clear that a fascinating scientific journey awaits us.

6. EPILOGUE

The mathematical logic of living in a world existing of 4 (classical) spacetime dimensions has guided me through the writing of this review: 1 section was devoted to introducing the reader to the 1D world of cool aging stars, and 3 sections to three different levels of 3D complexities; $1 + 3 = 4$. These 3D spatial complexities steer the 4D path through spacetime of any star.

This discourse brings us naturally to reflections on the next events that might occur on the 4D path, regarding not only the future of science in this field but also the future of the stars themselves. A 4D future in which the timescale of evolution of the 3D complexities cannot be considered as secular, and phenomena are not stationary; $\partial/\partial t \neq 0$. There are two prominent changes that I foresee occurring; the first one is within reach of the next few years, but the other might take substantially longer. First, there is the inclusion of binarity in both the forward theoretical and the retrieval modeling of the mass-loss rates of cool aging stars. This reorientation from a single-star perspective to the inclusion of (sub-)stellar companions will address the *how* question in a profound way. Second, the exploration of the 3D reality of gas-phase clusters for our

---

[7]The ESO press release—**https://www.eso.org/public/news/eso2003/**—was by far ESO's most popular press release of 2020, the study being covered in media outlets with a combined reach of over 2,300 million.

understanding of extraterrestrial dust formation is ripe with promise. This is an area within the field of astrochemistry where the *why* and *how* questions meet each other in an intimate way. For these two advances to occur, both the bottom-up and top-down approaches should be pursued in a collaborative effort among astrophysicists, laboratory experimentalists, and quantum chemists. In particular the bottom-up methodology might induce considerable progress in the field given the expected revolution in HPC facilities. I therefore express here the explicit desire for a more intense collaboration with computational experts and HPC facilities. Often we are too addicted to software codes inherited from the past, which are not adapted to current computer performances. That attitude limits the rate of progress in the field, and the rate of improving our understanding of the *how* and *why* questions.

This addressing of the *how* and *why* questions is only one small piece in a highly intricate puzzle. And just as you have the medium-sized Golden Russets and the large Haralsons apples, you have *why* and *Why* questions. I reserve the capital *Why* questions for these deeply grounded origins questions of which the (known) sample size is just one: Why did life emerge? and Why did the Universe come about? The *why* question addressed here enters a statistically very different domain with billions of stars exhibiting similar characteristics of old and simple, and at the same time of lively and creative as extraterrestrial laboratories. The link between the *whys* and the *Whys* can be expressed through the metaphor of Russian dolls, where each doll gives birth to a smaller doll, logically connected, seemingly separate, but never independent. This brings me to the very first sentences of this review: the *Why?*, *why?*, and *how?* questions driving the curiosity of the human race.

DISCLOSURE STATEMENT

ACKNOWLEDGMENTS

LITERATURE CITED

Adam C, Ohnaka K. 2019. *Astron. Astrophys.* 628:A132

Agúndez M, Cernicharo J, Guélin M. 2010. *Ap. J. Lett.* 724:L133–36

Agúndez M, Cernicharo J, Guélin M. 2014. *Astron. Astrophys.* 570:A45

Akerman CJ, Carigi L, Nissen PE, Pettini M, Asplund M. 2004. *Astron. Astrophys.* 414:931–42

Alfvén H. 1942. *Nature* 150:405–6

Arndt TU, Fleischer AJ, Sedlmayr E. 1997. *Astron. Astrophys.* 327:614–19

Arroyo-Torres B, Wittkowski M, Chiavassa A, et al. 2015. *Astron. Astrophys.* 575:A50

Auer LH, Woolf NJ. 1965. *Ap. J.* 142:182–88

Balick B, Frank A. 2002. *Annu. Rev. Astron. Astrophys.* 40:439–86

Baud B, Habing HJ. 1983. *Astron. Astrophys.* 127:73–83

Beasor ER, Davies B, Smith N, et al. 2020. *MNRAS* 492:5994–6006

Bennett PD. 2010. *Publ. Astron. Soc. Pac.* 425:181–90

Bergeat J, Chevallier L. 2005. *Astron. Astrophys.* 429:235–46

Bladh S, Liljegren S, Höfner S, Aringer B, Marigo P. 2019. *Astron. Astrophys.* 626:A100

Blöcker T. 1995. *Astron. Astrophys.* 297:727–38

Boersma C, Hony S, Tielens AGGM. 2006. *Astron. Astrophys.* 447:213–20

Bondi H, Hoyle F. 1944. *MNRAS* 104:273–82

Bose M, Floss C, Stadermann FJ. 2010. *Ap. J.* 714:1624–36

Boulangier J. 2019. *Developing a self-consistent AGB wind model*. PhD thesis, KU Leuven, Department of Physics and Astronomy

Boulangier J, Gobrecht D, Decin L, de Koter A, Yates J. 2019. *MNRAS* 489:4890–911

Bowen GH. 1988. *Ap. J.* 329:299–317

Bromley ST, Gómez Martín JC, Plane JMC. 2016. *Phys. Chem. Chem. Phys. (Incorporating Faraday Trans.)* 18:26913–22

Bujarrabal V, Alcolea J, Mikołajewska J, Castro-Carrizo A, Ramstedt S. 2018. *Astron. Astrophys.* 616:L3

Bujarrabal V, Castro-Carrizo A, Alcolea J, et al. 2016. *Astron. Astrophys.* 593:A92

Bujarrabal V, Castro-Carrizo A, Alcolea J, Sánchez Contreras C. 2001. *Astron. Astrophys.* 377:868–97

Bujarrabal V, Fuente A, Omont A. 1994. *Astron. Astrophys.* 285:247–71

Buscher DF, Haniff CA, Baldwin JE, Warner PJ. 1990. *MNRAS* 245:7P–11P

Cameron AGW. 1973. In *Interstellar Dust and Related Topics, Proc. IAU Symp. 52*, ed. JM Greenberg, HC van de Hulst, pp. 545–47. Dordrecht, Neth.: Reidel

Cannon E, Montargès M, de Koter A, Decin L, Min M, et al. 2021. *MNRAS*. 502:369–82

Cernicharo J, Cabezas C, Pardo JR, et al. 2019a. *Astron. Astrophys.* 630:L2

Cernicharo J, Marcelino N, Agúndez M, Guélin M. 2015. *Astron. Astrophys.* 575:A91

Cernicharo J, Velilla-Prieto L, Agúndez M, et al. 2019b. *Astron. Astrophys.* 627:L4

Chen M, Felmy AR, Dixon DA. 2014. *J. Phys. Chem. A* 118:3136–46

Chen Z, Frank A, Blackman EG, Nordhaus J, Carroll-Nellenback J. 2017. *MNRAS* 468:4465–77

Chen Z, Ivanova N, Carroll-Nellenback J. 2020. *Ap. J.* 892:110

Cherchneff I. 2006. *Astron. Astrophys.* 456:1001–12

Cherchneff I. 2011. *Astron. Astrophys.* 526:L11

Chiappini C, Romano D, Matteucci F. 2003. *MNRAS* 339:63–81

Choi BG, Huss GR, Wasserburg GJ, Gallino R. 1998. *Science* 282:1284–89

Cohen M, Van Winckel H, Bond HE, Gull TR. 2004. *Astron. J.* 127:2362–77

Cotton DV, Bailey J, Horta AD, Norris BRM, Lomax JR. 2020. *Res. Notes Am. Astron. Soc.* 4:39

Cox NLJ, Kerschbaum F, van Marle AJ, et al. 2012. *Astron. Astrophys.* 537:A35

Cuppen HM, Walsh C, Lamberts T, et al. 2017. *Space Sci. Rev.* 212:1–58

Curtis HD. 1918. *Publ. Lick Obs.* 13:57–74

Danilovich T, De Beck E, Black JH, Olofsson H, Justtanont K. 2016. *Astron. Astrophys.* 588:A119

Danilovich T, Gottlieb CA, Decin L, et al. 2020. *Ap. J.* 904:110

Danilovich T, Teyssier D, Justtanont K, et al. 2015. *Astron. Astrophys.* 581:A60

Davies B, Beasor ER. 2020a. *MNRAS* 493:468–76

Davies B, Beasor ER. 2020b. *MNRAS* 496:L142–46

Davis AM. 2011. *PNAS* 108:19142–46

De Beck E, Decin L, de Koter A, et al. 2010. *Astron. Astrophys.* 523:A18

De Beck E, Lombaert R, Agúndez M, et al. 2012. *Astron. Astrophys.* 539:A108

De Ceuster F, Bolte J, Homan W, et al. 2020a. *MNRAS* 499:5194–204

De Ceuster F, Homan W, Yates J, et al. 2020b. *MNRAS* 492:1812–26

de Jager C, Nieuwenhuijzen H, van der Hucht KA. 1988. *Astron. Astrophys. Suppl.* 72:259–89

de Mijolla D, Viti S, Holdship J, Manolopoulou I, Yates J. 2019. *Astron. Astrophys.* 630:A117

de Saint-Exupéry A. 1943. *Le Petit Prince*. Paris: Gallimard

Decin L, Cherchneff I, Hony S, et al. 2008. *Astron. Astrophys.* 480:431–38

Decin L, Cox NLJ, Royer P, et al. 2012. *Astron. Astrophys.* 548:A113

Decin L, Danilovich T, Gobrecht D, et al. 2018a. *Ap. J.* 855:113

Decin L, De Beck E, Brünken S, et al. 2010. *Astron. Astrophys.* 516:A69

Decin L, Homan W, Danilovich T, et al. 2019. *Nat. Astron.* 3:408–15

Decin L, Hony S, de Koter A, et al. 2006. *Astron. Astrophys.* 456:549–63

Decin L, Montargès M, Richards AMS, et al. 2020. *Science.* 369:1497–500

Decin L, Richards AMS, Danilovich T, Homan W, Nuth JA. 2018b. *Astron. Astrophys.* 615:A28

Decin L, Richards AMS, Millar TJ, et al. 2016. *Astron. Astrophys.* 592:A76

Decin L, Richards AMS, Neufeld D, et al. 2015. *Astron. Astrophys.* 574:A5

Decin L, Richards AMS, Waters LBFM, et al. 2017. *Astron. Astrophys.* 608:A55

Decin L, Royer P, Cox NLJ, et al. 2011. *Astron. Astrophys.* 534:A1

Demyk K, van Heijnsbergen D, von Helden G, Meijer G. 2004. *Astron. Astrophys.* 420:547–52

Deutsch AJ. 1956. *Ap. J.* 123:210–27

Dickens C. 1837. *The Posthumous Papers of the Pickwick Club, Containing a Faithful Record of the Perambulations, Perils, Travels, Adventures and Sporting Transactions of the Corresponding Members*. London: Chapman & Hall

Dominik C, Sedlmayr E, Gail HP. 1993. *Astron. Astrophys.* 277:578–94

Dyck HM, Benson JA, Ridgway ST, Dixon DJ. 1992. *Astron. J.* 104:1982–85

Eggleton PP. 1983. *Ap. J.* 268:368–69

Einstein A. 1905. *Ann. Phys.* 323:639–41

Einstein A. 1915. *Sitz. Königlich Preuß. Akad. Wiss. (Berlin)*. II:844–47

Ekström S, Georgy C, Eggenberger P, et al. 2012. *Astron. Astrophys.* 537:A146

El Mellah I, Bolte J, Decin L, Homan W, Keppens R. 2020. *Astron. Astrophys.* 637:A91

Eriksson K, Nowotny W, Höfner S, Aringer B, Wachter A. 2014. *Astron. Astrophys.* 566:A95

Feynman RP. 1959. *There's Plenty of Room at the Bottom: An Invitation to Enter a New Field of Physics*. Talk given at the annual meeting of the American Physical Society at the California Institute of Technology on Dec. 29, 1959. **https://www.zyvex.com/nanotech/feynman.html**

Flower DR, Pineau des Forêts G. 2015. *Astron. Astrophys.* 578:A63

Ford KES, Neufeld DA, Goldsmith PF, Melnick GJ. 2003. *Ap. J.* 589:430–38

Ford KES, Neufeld DA, Schilke P, Melnick GJ. 2004. *Ap. J.* 614:990–1006

Fox MW, Wood PR. 1982. *Ap. J.* 259:198–212

Freytag B, Höfner S, Liljegren S. 2019. In *Why Galaxies Care About AGB Stars: A Continuing Challenge through Cosmic Time, Proc. IAU Symp. 343*, ed. F Kerschbaum, M Groenewegen, H Olofsson, pp. 9–18. Cambridge, UK: Cambridge Univ. Press

Freytag B, Liljegren S, Höfner S. 2017. *Astron. Astrophys.* 600:A137

Freytag B, Steffen M, Dorch B. 2002. *Astron. Nachr.* 323:213–19

Fulton B. 2019. *Frequency of gaseous planets beyond the ice line*. Presented at Extreme Solar Systems IV, Reykjavik, Iceland

Fulton BJ, Petigura EA. 2018. *Astron. J.* 156:264

Gail HP, Sedlmayr E. 1999. *Astron. Astrophys.* 347:594–616

Gail HP, Sedlmayr E. 2013. *Physics and Chemistry of Circumstellar Dust Shells*. Cambridge, UK: Cambridge Univ. Press

García-Segura G, Langer N, Różyczka M, Franco J. 1999. *Ap. J.* 517:767–81

Gauger A, Gail HP, Sedlmayr E. 1990. *Astron. Astrophys.* 235:345–61

Gehrz RD, Woolf NJ. 1971. *Ap. J.* 165:285–94

Gillett FC, Low FJ, Stein WA. 1968. *Ap. J.* 154:677–87

Gilliland RL, Dupree AK. 1996. *Ap. J. Lett.* 463:L29–32

Gilman RC. 1969. *Ap. J. Lett.* 155:L185–87

Glass IS, Evans TL. 1981. *Nature* 291:303–4

Glassgold AE. 1999. In *Asymptotic Giant Branch Stars, Proc. IAU Symp. 191*, ed. T Le Bertre, A Lébre, C Waelkens, pp. 337–46. Cambridge, UK: Cambridge Univ. Press

Gobrecht D, Cherchneff I, Sarangi A, Plane JMC, Bromley ST. 2016. *Astron. Astrophys.* 585:A6

Gobrecht D, Cristallo S, Piersanti L, Bromley ST. 2017. *Ap. J.* 840:117

Gobrecht D, Decin L, Cristallo S, Bromley ST. 2018. *Chem. Phys. Lett.* 711:138–47

Godard B, Pineau des Forêts G, Lesaffre P, et al. 2019. *Astron. Astrophys.* 622:A100

Goderis S, Chakrabarti R, Debaille V, Kodolányi J. 2016. *J. Anal. At. Spectrom.* 31:841–62

Goldman SR, van Loon JT, Zijlstra AA, et al. 2017. *MNRAS* 465:403–33

Goldreich P, Scoville N. 1976. *Ap. J.* 205:144–54

Goumans TPM, Bromley ST. 2012. *MNRAS* 420:3344–49

Groenewegen MAT. 2014. *Astron. Astrophys.* 561:L11

Groenewegen MAT, Sloan GC, Soszyński I, Petersen EA. 2009. *Astron. Astrophys.* 506:1277–96

Groenewegen MAT, Vlemmings WHT, Marigo P, et al. 2016. *Astron. Astrophys.* 596:A50

Groh JH, Meynet G, Georgy C, Ekström S. 2013. *Astron. Astrophys.* 558:A131

Grossman L, Larimer JW. 1974. *Rev. Geophys. Space Phys.* 12:71–101

Guélin M, Patel NA, Bremer M, et al. 2018. *Astron. Astrophys.* 610:A4

Guerrero MA, Chu YH, Manchado A, Kwitter KB. 2003. *Astron. J.* 125:3213–21

Gustafsson B, Höfner S. 2003. In *Asymptotic Giant Branch Stars*, ed. HJ Habing, H Olofsson, pp. 149–245. New York/Berlin: Springer

Haniff CA, Buscher DF. 1998. *Astron. Astrophys.* 334:L5–8

Henning T. 2010. *Annu. Rev. Astron. Astrophys.* 48:21–46

Heras AM, Hony S. 2005. *Astron. Astrophys.* 439:171–82

Hertzsprung E. 1905. *Z. Wiss. Photogr.* 3:442–49

Hertzsprung E. 1911. *Publ. Astrophys. Obs. Potsdam* 22:A1–40.1

Hinkle KH, Aringer B, Lebzelter T, Martin CL, Ridgway ST. 2000. *Astron. Astrophys.* 363:1065–80

Höfner S. 2008. *Astron. Astrophys.* 491:L1–4

Höfner S, Andersen AC. 2007. *Astron. Astrophys.* 465:L39–42

Höfner S, Bladh S, Aringer B, Ahuja R. 2016. *Astron. Astrophys.* 594:A108

Höfner S, Feuchtinger MU, Dorfi EA. 1995. *Astron. Astrophys.* 297:815–27

Höfner S, Freytag B. 2019. *Astron. Astrophys.* 623:A158

Höfner S, Olofsson H. 2018. *Astron. Astrophys. Rev.* 26:1

Hohenberg P, Kohn W. 1964. *Phys. Rev.* 136:864–71

Homan W, Danilovich T, Decin L, et al. 2018a. *Astron. Astrophys.* 614:A113

Homan W, Richards A, Decin L, de Koter A, Kervella P. 2018b. *Astron. Astrophys.* 616:A34

Hoyle F, Lyttleton RA. 1939. *Proc. Camb. Philos. Soc.* 35:405–15

Hoyle F, Wickramasinghe NC. 1962. *MNRAS* 124:417–33

Ivanova N, Justham S, Chen X, et al. 2013. *Astron. Astrophys. Rev.* 21:59

Jaeger C, Molster FJ, Dorschner J, et al. 1998. *Astron. Astrophys.* 339:904–16

Jeffers SV, Min M, Waters LBFM, et al. 2014. *Astron. Astrophys.* 572:A3

Jeong KS, Chang C, Sedlmayr E, Sülze D. 2000. *J. Phys. B At. Mol. Phys.* 33:3417–30

Jeong KS, Winters JM, Le Bertre T, Sedlmayr E. 2003. *Astron. Astrophys.* 407:191–206

Josselin E, Plez B. 2007. *Astron. Astrophys.* 469:671–80

Justtanont K, Feuchtgruber H, de Jong T, et al. 1998. *Astron. Astrophys.* 330:L17–20

Kamiński T. 2019. *Astron. Astrophys.* 627:A114

Kamiński T, Müller HSP, Schmidt MR, et al. 2017. *Astron. Astrophys.* 599:A59

Karovicova I, Wittkowski M, Ohnaka K, et al. 2013. *Astron. Astrophys.* 560:A75

Karovska M, Nisenson P, Beletic J. 1993. *Ap. J.* 402:311–13

Kee N, Sundqvist J, Decin L, de Koter A, Sana H. 2021. *Astron. Astrophys.* 646:A180

Kervella P, Gallenne A, Remage Evans N, et al. 2019. *Astron. Astrophys.* 623:A116

Kervella P, Homan W, Richards AMS, et al. 2016. *Astron. Astrophys.* 596:A92

Khouri T, Maercker M, Waters LBFM, et al. 2016. *Astron. Astrophys.* 591:A70

Khouri T, Waters LBFM, de Koter A, et al. 2015. *Astron. Astrophys.* 577:A114

Kim H, Liu SY, Hirano N, et al. 2015. *Ap. J.* 814:61

Kim H, Liu SY, Taam RE. 2019. *Ap. J. Suppl.* 243:35

Kim H, Taam RE. 2012. *Ap. J.* 759:59

Kochanek CS, Khan R, Dai X. 2012. *Ap. J.* 759:20

Kristyan S. 2013. *J. Theor. Appl. Phys.* 7:61

Lagadec E, Zijlstra AA. 2008. *MNRAS* 390:L59–63

Lamers HJGLM, Cassinelli JP. 1999. *Introduction to Stellar Winds*. Cambridge, UK: Cambridge Univ. Press

Lamiel-Garcia O, Cuko A, Calatayud M, Illas F, Bromley ST. 2017. *Nanoscale* 9:1049–58

Lee G, Helling C, Giles H, Bromley ST. 2015. *Astron. Astrophys.* 575:A11

Lee GKH, Blecic J, Helling C. 2018. *Astron. Astrophys.* 614:A126

Lesaffre P, Pineau des Forêts G, Godard B, et al. 2013. *Astron. Astrophys.* 550:A106

Lewis RS, Ming T, Wacker JF, Anders E, Steel E. 1987. *Nature* 326:160–62

Li R, Cheng L. 2012. *Comput. Theor. Chem.* 996:125–31

Li X, Millar TJ, Walsh C, Heays AN, van Dishoeck EF. 2014. *Astron. Astrophys.* 568:A111

Liljegren S, Höfner S, Freytag B, Bladh S. 2018. *Astron. Astrophys.* 619:A47

Liu ZW, Stancliffe RJ, Abate C, Matrozis E. 2017. *Ap. J.* 846:117

Lodders K, Amari S. 2005. *Chem. Erde/Geochem.* 65:93–166

Lombaert R, Decin L, Royer P, et al. 2016. *Astron. Astrophys.* 588:A124

Maercker M, Mohamed S, Vlemmings WHT, et al. 2012. *Nature* 490:232–34

Martínez L, Santoro G, Merino P, et al. 2020. *Nat. Astron.* 4:97–105

Mastrodemos N, Morris M. 1999. *Ap. J.* 523:357–80

Matsuura M, Sloan GC, Zijlstra AA, et al. 2007. *Publ. Astron. Soc. Pac.* 378:450–55

Mauney C, Buongiorno Nardelli M, Lazzati D. 2015. *Ap. J.* 800:30

Mauron N, Huggins PJ. 1999. *Astron. Astrophys.* 349:203–8

Mauron N, Huggins PJ. 2006. *Astron. Astrophys.* 452:257–68

Maury AC, Pickering EC. 1897. *Ann. Harv. Coll. Obs.* 28:1–128

McDonald I, Trabucchi M. 2019. *MNRAS* 484:4678–82

McDonald I, Zijlstra AA. 2015. *MNRAS* 448:502–21

McDonald I, Zijlstra AA. 2016. *Ap. J. Lett.* 823:L38

McGuire BA. 2018. *Ap. J. Suppl.* 239:17

Melnick GJ, Neufeld DA, Ford KES, Hollenbach DJ, Ashby MLN. 2001. *Nature* 412:160–63

Menut JL, Gendron E, Schartmann M, et al. 2007. *MNRAS* 376:L6–10

Mihalas D, Hummer DG. 1974. *Ap. J. Suppl.* 28:343–72

Miszalski B, Acker A, Moffat AFJ, Parker QA, Udalski A. 2009. *Astron. Astrophys.* 496:813–25

Moe M, Di Stefano R. 2017. *Ap. J. Suppl.* 230:15

Molster FJ, Waters LBFM, Tielens AGGM, Barlow MJ. 2002. *Astron. Astrophys.* 382:184–221

Molster FJ, Waters LBFM, Trams NR, et al. 1999a. *Astron. Astrophys.* 350:163–80

Molster FJ, Yamamura I, Waters LBFM, et al. 1999b. *Nature* 401:563–65

Montargès M, Cannon E, Lagadec E, et al. 2021. *Nature*. In press. **http://hdl.handle.net/10871/125362**

Montargès M, Homan W, Keller D, et al. 2019. *MNRAS* 485:2417–30

Neri R, Kahane C, Lucas R, Bujarrabal V, Loup C. 1998. *Astron. Astrophys. Suppl.* 130:1–64

Nielsen EL, De Rosa RJ, Macintosh B, et al. 2019. *Astron. J.* 158:13

Nieuwenhuijzen H, de Jager C. 1990. *Astron. Astrophys.* 231:134–36

Nittler LR, Alexander CMO, Gallino R, et al. 2008. *Ap. J.* 682:1450–78

Nittler LR, Ciesla F. 2016. *Annu. Rev. Astron. Astrophys.* 54:53–93

Norris BR, Tuthill PG, Ireland MJ, et al. 2012. *Nature* 484:220–22

O'Dell CR, Balick B, Hajian AR, Henney WJ, Burkert A. 2002. *Astron. J.* 123:3329–47

O'Dell CR, McCullough PR, Meixner M. 2004. *Astron. J.* 128:2339–56

O'Gorman E, Kervella P, Harper GM, et al. 2017. *Astron. Astrophys.* 602:L10

Ohnaka K. 2014. *Astron. Astrophys.* 568:A17

Ohnaka K, Driebe T, Hofmann KH, et al. 2006. *Astron. Astrophys.* 445:1015–29

Ohnaka K, Weigelt G, Hofmann KH. 2017a. *Astron. Astrophys.* 597:A20

Ohnaka K, Weigelt G, Hofmann KH. 2017b. *Nature* 548:310–12

Olofsson H. 2005. In *Astrochemistry: Recent Successes and Current Challenges, Proc. IAU Symp. 231*, ed. DC Lis, GA Blake, E Herbst, pp. 499–508. Cambridge, UK: Cambridge Univ. Press

Olofsson H, Maercker M, Eriksson K, Gustafsson B, Schöier F. 2010. *Astron. Astrophys.* 515:A27

Onaka T, de Jong T, Willems FJ. 1989. *Astron. Astrophys.* 218:169–79

Paczyński B. 1970. *Acta Astron.* 20:47–58

Paczyński B. 1971. *Annu. Rev. Astron. Astrophys.* 9:183–208

Paladini C, Baron F, Jorissen A, et al. 2018. *Nature* 553:310–12

Parker EN. 1958. *Ap. J.* 128:664–76

Parker EN. 1960. *Ap. J.* 132:821–66

Parker QA, Acker A, Frew DJ, et al. 2006. *MNRAS* 373:79–94

Patzer A. 1998. *Non-equilibrium effects on chemistry and dust formation in circumstellar outflows*. Ph.D. thesis, Tech. Univ. Berlin

Podsiadlowski P, Mohamed S. 2007. *Balt. Astron.* 16:26–33

Poe EA. 1845. In *Graham's Magazine*. 28(5):193–200

Ramstedt S, Maercker M, Olofsson G, Olofsson H, Schöier FL. 2011. *Astron. Astrophys.* 531:A148

Ramstedt S, Mohamed S, Olander T, et al. 2018. *Astron. Astrophys.* 616:A61

Ramstedt S, Mohamed S, Vlemmings WHT, et al. 2014. *Astron. Astrophys.* 570:L14

Ramstedt S, Schöier FL, Olofsson H, Lundgren AA. 2008. *Astron. Astrophys.* 487:645–57

Randall SK, Trejo A, Humphreys EML, et al. 2020. *Astron. Astrophys.* 636:A123

Reimers D. 1975. *Mem. Soc. R. Sci. Liege* 8:369–82

Renzini A. 1981. In *Physical Processes in Red Giants*, ed. I Eben, A Renzini. *Ap. Space Sci. Libr.* 88:431–46. Dordrecht, Neth.: Springer

Ryde N, Eriksson K, Gustafsson B, Lindqvist M, Olofsson H. 1998. *Ap. Space Sci.* 255:301–2

Sabach E, Soker N. 2018. *MNRAS* 479:2249–55

Safonov B, Dodin A, Burlak M, et al. 2020. arXiv:2005.05215

Sahai R, Morris MR, Villar GG. 2011. *Astron. J.* 141:134

Saladino MI, Pols OR. 2019. *Astron. Astrophys.* 629:A103

Saladino MI, Pols OR, van der Helm E, Pelupessy I, Portegies Zwart S. 2018. *Astron. Astrophys.* 618:A50

Salasnich B, Bressan A, Chiosi C. 1999. *Astron. Astrophys.* 342:131–52

Sana H, de Mink SE, de Koter A, et al. 2012. *Science* 337:444–46

Schöier FL, Olofsson H, Lundgren AA. 2006. *Astron. Astrophys.* 454:247–55

Schöier FL, Ramstedt S, Olofsson H, et al. 2013. *Astron. Astrophys.* 550:A78

Schöier FL, Ryde N, Olofsson H. 2002. *Astron. Astrophys.* 391:577–86

Schröder KP, Smith RC. 2008. *MNRAS* 386:155–63

Schwarzschild M. 1975. *Ap. J.* 195:137–44

Scicluna P, Siebenmorgen R, Wesson R, et al. 2015. *Astron. Astrophys.* 584:L10

Shawl SJ. 1972. *Observations and Models of Polarization in Late - Stars*. PhD Thesis, Univ. Texas at Austin

Simis YJW, Icke V, Dominik C. 2001. *Astron. Astrophys.* 371:205–21

Smartt SJ, Eldridge JJ, Crockett RM, Maund JR. 2009. *MNRAS* 395:1409–37

Smolders K, Acke B, Verhoelst T, et al. 2010. *Astron. Astrophys.* 514:L1

Soker N. 1998. *Ap. J.* 496:833–41

Soker N. 2001. *Ap. J.* 558:157–64

Soker N, Harpaz A. 1992. *Publ. Astron. Soc. Pac.* 104:923

Solomon P, Jefferts KB, Penzias AA, Wilson RW. 1971. *Ap. J. Lett.* 163:L53–56

Srinivasan S, Meixner M, Leitherer C, Vijh U, Volk K, et al. 2009. *Astron. J.* 137:4810–23

Straniero O, Chieffi A, Limongi M, et al. 1997. *Ap. J.* 478:332–39

Stroud RM, Nittler LR, Alexander CMO. 2004. *Science* 305:1455–57

Su KYL, Chu YH, Rieke GH, et al. 2007. *Ap. J. Lett.* 657:L41–45

Tielens AGGM. 1990. In *From Miras to Planetary Nebulae: Which Path for Stellar Evolution?*, ed. MO Mennessier, A Omont. Lausanne, Switz.: Editions Frontiéres

Tielens AGGM. 2005. *The Physics and Chemistry of the Interstellar Medium*. Cambridge, UK: Cambridge Univ. Press

Tielens AGGM, Waters LBFM, Molster FJ, Justtanont K. 1998. *Ap. Space Sci.* 255:415–26

Trabucchi M, Wood PR, Montalbán J, et al. 2017. *Ap. J.* 847:139

Trabucchi M, Wood PR, Montalbán J, et al. 2019. *MNRAS* 482:929–49

Ueta T, Murakawa K, Meixner M. 2007. *Astron. J.* 133:1345–60

Van de Sande M, Decin L, Lombaert R, et al. 2018a. *Astron. Astrophys.* 609:A63

Van de Sande M, Millar TJ. 2019. *Ap. J.* 873:36

Van de Sande M, Sundqvist JO, Millar TJ, et al. 2018b. *Astron. Astrophys.* 616:A106

van Loon JT, Cioni MRL, Zijlstra AA, Loup C. 2005. *Astron. Astrophys.* 438:273–89

van Marle AJ, Meliani Z, Keppens R, Decin L. 2011. *Ap. J. Lett.* 734:L26

Vassiliadis E, Wood PR. 1993. *Ap. J.* 413:641–57

Velilla Prieto L, Cernicharo J, Quintana-Lacaci G, et al. 2015. *Ap. J. Lett.* 805:L13

Verhoelst T, van der Zypen N, Hony S, et al. 2009. *Astron. Astrophys.* 498:127–38

Walmswell JJ, Eldridge JJ. 2012. *MNRAS* 419:2054–62

Waters LBFM, Molster FJ, Hony S, et al. 2000. *Publ. Astron. Soc. Pac.* 196:3–14

Weaver H, Williams DRW, Dieter NH, Lum WT. 1965. *Nature* 208:29–31

Weigelt G, Balega Y, Bloecker T, et al. 1998. *Astron. Astrophys.* 333:L51–54

Weinberg S. 1994. *Dreams of a Final Theory*. New York: Vintage

Weymann R. 1962a. *Ap. J.* 136:476–86

Weymann R. 1962b. *Ap. J.* 136:844–65

Wickramasinghe NC, Donn BD, Stecher TP. 1966. *Ap. J.* 146:590–92

Wiegert J, Groenewegen MAT, Jorissen A, Decin L, Danilovich T. 2020. *Astron. Astrophys.* 642:A142

Wildt R. 1933. *Z. Astrophys.* 6:345–54

Willacy K, Cherchneff I. 1998. *Astron. Astrophys.* 330:676–84

Willacy K, Millar TJ. 1997. *Astron. Astrophys.* 324:237–48

Willson LA. 2000. *Annu. Rev. Astron. Astrophys.* 38:573–611

Wilson WJ, Barrett AH. 1968. *Science* 161:778–79

Wittgenstein L. 1921. *Tractatus Logico-Philosophicus*. New York: Harcourt, Brace & Co.

Wittkowski M, Hofmann KH, Höfner S, et al. 2017. *Astron. Astrophys.* 601:A3

Woitke P. 2006a. *Astron. Astrophys.* 452:537–49

Woitke P. 2006b. *Astron. Astrophys.* 460:L9–12

Wong KT, Kamiński T, Menten KM, Wyrowski F. 2016. *Astron. Astrophys.* 590:A127

Wood PR. 1990. *Publ. Astron. Soc. Pac.* 11:355–64

Wood PR. 2015. *MNRAS* 448:3829–43

Wood PR, Alcock C, Allsman RA, et al. 1999. In *Asymptotic Giant Branch Stars*, *Proc. IAU Symp. 191*, ed. T Le Bertre, A Lébre, C Waelkens, pp. 151–58. Cambridge, UK: Cambridge Univ. Press

Woolf NJ, Ney EP. 1969. *Ap. J. Lett.* 155:L181–84

Woosley SE, Heger A. 2012. *Ap. J.* 752:32

Yoon SC, Cantiello M. 2010. *Ap. J. Lett.* 717:L62–65

Zhang B, Reid MJ, Menten KM, Zheng XW. 2012. *Ap. J.* 744:23

Zijlstra AA, Lagadec E, Sloan G, Matsuura M. 2009. *Publ. Astron. Soc. Pac.* 412:65–80